Parametric Study of Transient Dynamics of Multitransmitter Dynamic Wireless Power Transfer for Linear Transport Systems

Junyi Ji, Chong Zhu, *Member, IEEE*, Jia Li, *Graduate Student Member, IEEE*, Jixie Xie, and Xi Zhang, *Senior Member, IEEE*

***Abstract*—Dynamic wireless power transfer (DWPT) addresses the power supply limitations of magnetically levitated transport systems reliant on rigid cables, yet receiver motion introduces undesirable power fluctuations due to transient coupling variations between segmented transmitters and receivers. While prior studies focus on steady-state output dependence on coil positions, they overlook transient dynamics under multicoupling changes. This article bridges this gap by developing a transient model using the extended describing function method to capture multi-coupling effects, extracting dominant poles and mode frequencies. By decomposing nonlinear coupling coefficient variations into sinusoidal inputs linked to motion speed, the model reveals that the dominant mode frequency significantly exceeds the coupling variation frequency, suggesting a response closely aligned with steady-state behavior. This enables a detailed parametric study of motion speed, output filter capacitance, start-up acceleration, input voltage, and load resistance, precisely quantifying their impacts on inverter current fluctuations and output voltage stability across diverse operating conditions. Experimental results obtained under various values of these parameters on a DWPT test platform demonstrate strong agreement with the model predictions. These findings confirm the model's accuracy and practical value for guiding system design and improving overall performance.**

***Index Terms*—Dynamic wireless power transfer (DWPT), linear transport system, transient analysis.**

I. Introduction

MAGNETICALLY levitated transport systems, as a novel linear transportation solution, offer high precision, low noise, and reduced maintenance, making them ideal for semiconductor and printed circuit board manufacturing [1], [2]. However, using rigid power cables restricts flexibility and increases wear. As shown in Fig. 1, dynamic wireless power transfer (DWPT) alleviates these issues by sequentially placing transmitter coils along the track to wirelessly power the levitated mover, thus eliminating cables and simplifying maintenance [3], [4], [5], [6].

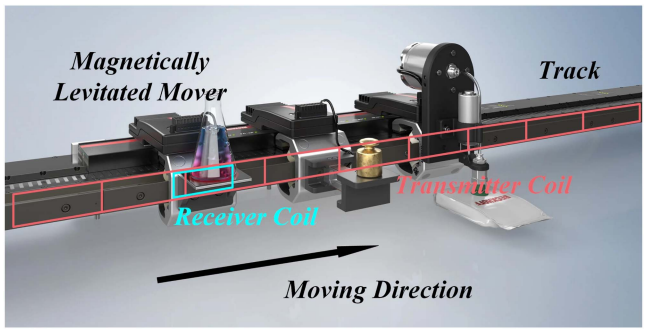

Fig. 1. Magnetic levitated transport system with dynamic wireless power transfer for mover power supply [3].

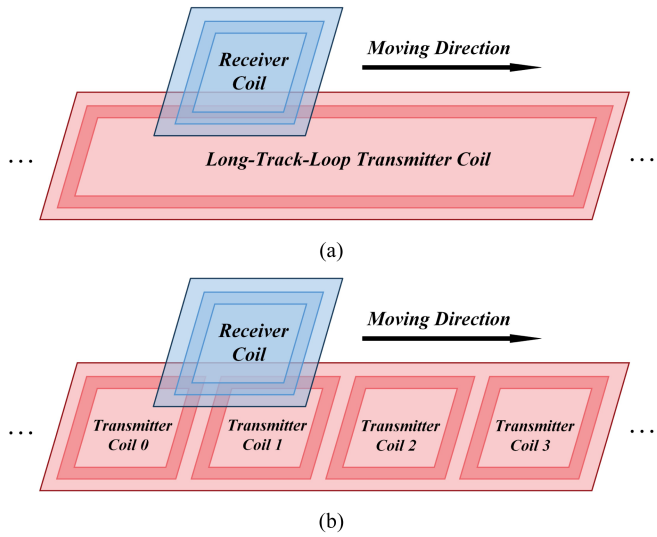

Fig. 2. Common DWPT structures. (a) Long-track-loop structure. (b) Short-individual structure.

Existing DWPT systems predominantly adopt either a long-track-loop structure [7], [8] or a short-individual structure [9], [10], [11], as shown in Fig. 2. Unlike the long-track-loop design, where the transmitter coil is typically tens of times longer than the receiver coil, the short-individual structure features transmitter coils with lengths generally ranging from one to several

Received 9 April 2025; revised 30 June 2025; accepted 27 July 2025. Date of publication 7 August 2025; date of current version 22 October 2025. This work was supported by the National Natural Science Foundation of China under Grant 52377210. Recommended for publication by Associate Editor S. Jeong. *(Corresponding author: Chong Zhu.)*

The authors are with the School of Mechanical Engineering, Shanghai Jiao Tong University, Shanghai 200240, China (e-mail: jijunyi@sjtu.edu.cn; chong.zhu@sjtu.edu.cn; 18852647159@sjtu.edu.cn; xiejixie@sjtu.edu.cn; braver1980@sjtu.edu.cn).

Color versions of one or more figures in this article are available at https://doi.org/10.1109/TPEL.2025.3596911.

Digital Object Identifier 10.1109/TPEL.2025.3596911

times that of the receiver coil. The short-individual design allows more continuous and stable power transfer, reduces parasitic resistance and electromagnetic interference [12], and allocates an independent compensation network to each transmitter coil. Such a configuration improves efficiency, streamlines maintenance, and enhances scalability [9], making short-individual design well-suited for linear transport. However, in this scenario, the coupling coefficient between transmitter and receiver coils varies with their relative positions, causing voltage and current fluctuations [13], [14]. Overcurrent stresses the switching devices, while high voltages on coils and resonant capacitances may damage components or compromise system stability. Addressing these risks often requires higher-rated devices, raising overall costs.

Although numerous control strategies have been proposed to mitigate these fluctuations, most rely on steady-state or quasi-steady-state models [15], [16], [17], [18], [19], which treat the static operating value under each position-dependent coupling coefficient as the transient operating point of the DWPT system. Such approaches assume slow or constant coupling variations and do not adequately capture the transient behavior induced by receiver coil motion or rectifier dynamics. Additionally, unlike electric vehicles demanding constant-current output, linear transport systems require constant-voltage output, which entails higher sensitivity to parameter variations and narrower tolerance margins.

Key factors influencing the transient response include motion speed, start-up acceleration, output filter capacitance, input voltage, and load resistance. The output capacitance determines the smoothness of the output voltage and current, while the motion speed affects the frequency of coupling coefficient variations. Frequent start-stop operations highlight the role of start-up acceleration in shaping the initial transient process. Variations in input voltage directly influence the system's overall energy level and the amplitude of dynamic responses, whereas load resistance determines the output power demand and further affects inverter current fluctuations and voltage stability. However, existing studies [15], [16], [17], [18], [19] have paid insufficient attention to the effects of these parameters on the output characteristics, and motion-induced transients remain inadequately explored.

Hence, an appropriate transient model is essential for accurately representing DWPT system dynamics during the movement of the receiver coil. Most existing WPT modeling studies focus on static scenarios [20], [21], [22], [23]. Methods based on large-signal models [21], [24] can capture comprehensive nonlinear switching characteristics and handle wide-range disturbances, but often entail high computational costs and complex simulations, especially for multi-coil systems with rapidly varying coupling. They also lack a clear frequency-domain perspective for stability analysis. Meanwhile, envelope models assume ideal resonance and ignore high-frequency harmonics [25], thus simplifying slow-varying envelope analysis. However, these models lose accuracy under detuning and still require linearization for control design. Furthermore, these approaches primarily incorporate inputs such as voltage, duty cycle, load, or switching frequency, without in-depth examination of how coupling coefficient variations during motion affect system performance.

Li et al., [26] introduced "coupling coefficient sensitivity" to investigate transient effects under step changes in coupling, but that work remains limited to single-transmitter configurations. It does not address the modeling complexity that arises when multiple coils and mutual coupling paths substantially increase system order, nor does it consider the influences of the circuit parameters or motion speed. Liu et al., [27] derived the transfer function model relating receiver coil voltage to receiver coil current and rectifier input voltage based on near-constant transmitter coil current and an ideal resonant phase assumption, without accounting for the transient response on the transmitter side. Moreover, similar to [24], that study primarily analyzed the effects of the motion speed through experimental observations or simulation, lacking an appropriate analytical framework to quantitatively assess how the motion speed impacts system dynamics.

In summary, it is imperative to develop a transient model that accurately simulates the response of multitransmitter DWPT systems to positional variations between the receiver coil and multiple transmitter coils. Such a model should theoretically establish a link between motion speed and dynamic characteristics, thereby elucidating system response under various motion speeds and circuit configurations. To address these challenges, this article proposes a small-signal model for multitransmitter DWPT systems that treats cross-coupling coefficients as system inputs, preserving the essential coupling dynamics. Furthermore, we employ Fourier decomposition to convert the nonlinear variations in coupling coefficients into sinusoidal inputs that are correlated with the receiver coil's motion speed, thus determining the highest frequency of the input signal. Our analysis reveals that the dominant modal frequency is significantly higher than the frequency of coupling variations, indicating that the overall system response closely approximates steady-state behavior.

By leveraging this low-frequency approximation, we apply frequency-domain techniques to conduct a detailed parametric study of motion speed, output filter capacitance, start-up acceleration, input voltage, and load resistance. This analysis quantitatively evaluates their impacts on inverter output current fluctuations and rectifier output voltage stability with high precision. The results indicate that these parameters all have significant effects on the inverter output current, with the fluctuation amplitude exhibiting linear correlations with each parameter. In contrast, the rectifier output voltage is primarily affected by input voltage and remains largely insensitive to variations in the other parameters. Experimental results obtained from a DWPT test platform with controllable speed and start-up acceleration, and conducted across a wide range of parameter values, show strong agreement with the model predictions, further confirming the accuracy and practical value of the proposed approach in improving system performance.

Overall, by integrating speed effects into the transient model, this study elucidates DWPT systems' output fluctuation mechanisms and evaluates how key parameters govern system dynamics. Experimental findings confirm the model's effectiveness in

capturing parameter-dependent responses. The main contributions are as follows.

1) Developed a transient model for multitransmitter coil LCC-S topology DWPT systems based on the extended describing function (EDF) method, enabling the capture of multicoupling effects.
2) Proposed a frequency-domain analysis framework based on Fourier decomposition that correlates motion speed with system input frequency, thereby enabling accurate transient response prediction and analysis.
3) Identified the impacts of motion speed, start-up acceleration, output filter capacitance, input voltage, and load resistance on inverter output current i_f fluctuations and rectifier output voltage v_{out} stability, offering reliable reference for parameter design in DWPT systems.

II. Dynamic Analysis of the DWPT System

In short-individual DWPT systems, multiple transmitter coils are installed beneath the track. As the receiver coil moves along the path, it primarily couples with the two nearest transmitter coils, while the coupling with other coils can be neglected [27]. Meanwhile, to improve system efficiency, the transmitter coils are sequentially activated and deactivated based on detection signals, typically following a switching strategy in which no more than two coils are energized at any given time [28], [29]. As a result, the entire DWPT process can be regarded as a continuous repetition of the receiver coil moving from the center of one transmitter coil to the center of the next, thereby enabling stable power delivery. Hence, the system exhibits modularity and periodicity. Based on this observation, this article simplifies the modeling process and reduces computational complexity by analyzing the coupling behavior among two transmitter coils and one receiver coil within a single motion cycle.

Currently, common compensation network topologies for WPT include series–series (SS), series–parallel (S-P), parallel–parallel (P-P), double-sided inductor-capacitor-capacitor (*LCC*), and inductor-capacitor-capacitor-series (LCC-S) compensation topologies [30], [31], [32]. Among these, LCC-S topology is particularly suitable for WPT systems with multiple transmitting coils because it offers higher design flexibility and reduces current stress [33]. Meanwhile, the constant voltage output characteristic of the LCC-S topology can also meet the power supply requirements of the linear transport system. Therefore, this article chooses the LCC-S topology to investigate the short-individual DWPT system. The modeling and analysis methods presented can also be applied to other topological structures.

Fig. 3 shows the multitransmitter LCC-S DWPT system, including two transmitter coils and one receiver coil. The two transmitters have the same compensation topology. L_{p1}, L_{p2}, and L_s represent the self-inductance of the two transmitter coils and the receiver coil, respectively. R_{p1}, R_{p2}, and R_s are the internal resistances of the corresponding coils. M_1 and M_2 represent the mutual inductance between each transmitter coil and the receiver coil, while M_p represents the mutual inductance between the two transmitter coils. L_{f1}, C_{f1}, C_{p1}, L_{f2}, C_{f2}, and C_{p2} form the *LCC* compensation networks for the two transmitter coils. C_s is the

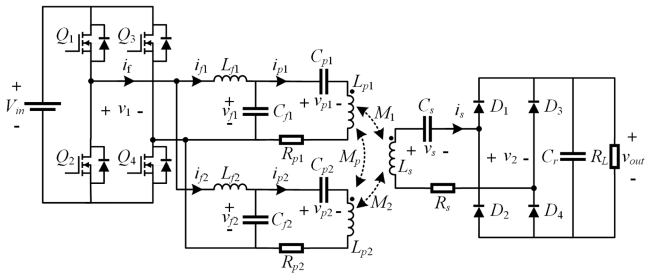

Fig. 3. Circuit topology of LCC-S DWPT system.

compensation capacitance for the receiver coil. C_r is the output filter capacitance. R_L is the load resistor. The ON-resistance of the MOSFETS Q_1–Q_4 on the primary side is R_{ds}. The forward voltage drop of the rectifier diodes D_1–D_4 on the secondary side is V_F. i_{p1} and i_{p2} are the currents through the two transmitter coils. i_{f1} and i_{f2} are the currents through L_{f1} and L_{f2}, respectively. i_f is the output current of the full bridge inverter. i_s is the input current of the rectifier. v_1 is the output voltage of the rectifier. v_2 is the input voltage of the full bridge inverter. v_{f1} and v_{f2} are the voltages across C_{f1} and C_{f2}, respectively. v_{p1} and v_{p2} are the voltages across C_{p1} and C_{p2}, respectively, while v_s is the voltage across C_s. v_{Cr} is the voltage across C_r, which is also the load voltage v_{out}. V_{in} is the power supply voltage. Considering the modular design of the system, we define $L_{\text{f1}} = L_{f2} = L_f$, $C_{f1} = C_{f2} = C_f$, $C_{p1} = C_{p2} = C_p$, $L_{p1} = L_{p2} = L_p$, and $R_{p1} = R_{p2} = R_p$.

A. Nonlinear State-Space Equations

Applying KVL to the circuit in Fig. 3, the following is obtained:

$$\begin{cases} L_f i'_{f1} = v_1 - v_{f1} - 2R_{\text{ds}}\left(i_{f1} + i_{f2}\right) \\ L_f i'_{f2} = v_1 - v_{f2} - 2R_{\text{ds}}\left(i_{f1} + i_{f2}\right) \\ L_p i'_{p1} - M_1 i'_s + M_p i'_{p2} = v_{f1} - v_{p1} - R_p i_{p1} \\ L_p i'_{p2} - M_2 i'_s + M_p i'_{p1} = v_{f2} - v_{p2} - R_p i_{p2} \\ M_1 i'_{p1} + M_2 i'_{p2} - L_s i'_s = v_s + v_2 + R_s i_s \end{cases}. \tag{1}$$

Mutual inductances are expressed in terms of the coupling coefficients as follows:

$$\begin{cases} M_1 = k_1\sqrt{L_p L_s} \\ M_2 = k_2\sqrt{L_p L_s} \\ M_p = k_p L_p \end{cases}. \tag{2}$$

Substituting (2) into (1), the solutions can be obtained as follows:

$$\begin{cases} i'_{f1} = \left[v_1 - v_{f1} - 2R_{ds}\left(i_{f1} + i_{f2}\right)\right]/L_f \\ i'_{f2} = \left[v_1 - v_{f2} - 2R_{ds}\left(i_{f1} + i_{f2}\right)\right]/L_f \\ i'_{p1} = \left[\left(1-k_2^2\right)L_s v_{\text{eq1}} + \left(k_1 k_2 - k_p\right)L_s v_{\text{eq2}} \right. \\ \qquad \left. + \left(k_1 - k_2 k_p\right)\sqrt{L_p L_s}\, v_{\text{eq0}}\right]/L_{\text{eqm}} \\ i'_{p2} = \left[\left(1-k_1^2\right)L_s v_{\text{eq2}} + \left(k_1 k_2 - k_p\right)L_s v_{\text{eq1}} \right. \\ \qquad \left. + \left(k_2 - k_1 k_p\right)\sqrt{L_p L_s}\, v_{\text{eq0}}\right]/L_{\text{eqm}} \\ i'_s = \left\{\sqrt{L_p L_s}\left[\left(k_1 - k_2 k_p\right)v_{\text{eq1}} + \left(k_2 - k_1 k_p\right)v_{\text{eq2}}\right] \right. \\ \qquad \left. + \left(1-k_p^2\right)L_p v_{\text{eq0}}\right\}/L_{\text{eqm}} \end{cases} \tag{3}$$

where

$$\begin{cases} v_{\text{eq1}} = R_p i_{p1} + v_{p1} - v_{f1} \\ v_{\text{eq2}} = R_p i_{p2} + v_{p2} - v_{f2} \\ v_{\text{eq0}} = v_s + v_2 + R_s i_s \\ L_{\text{eq}m} = -\left(1 - k_1^2 - k_2^2 + 2k_1k_2k_p - k_p^2\right) L_p L_s \end{cases}. \tag{4}$$

Applying KCL to the circuit in Fig. 3, the following is obtained:

$$\begin{cases} v'_{f1} = \frac{(i_{f1} - i_{p1})}{C_f} \\ v'_{f2} = \frac{(i_{f2} - i_{p2})}{C_f} \\ v'_{p1} = \frac{i_{p1}}{C_p} \\ v'_{p2} = \frac{i_{p2}}{C_p} \\ v'_s = \frac{i_s}{C} \\ v'_{Cr} = \frac{|i_s|}{C_r} - \frac{v_{Cr}}{C_r R_L} \end{cases}. \tag{5}$$

Equations (3) and (5) together constitute an accurate nonlinear state-space model of the LCC-S DWPT system shown in Fig. 3.

B. Harmonic Approximation

The state-space representation mentioned above contains both linear and nonlinear terms. However, due to the presence of ac components, it is difficult to locally linearize the state equations to obtain a small-signal model. The state variables in the compensation network exhibit nearly sinusoidal waveforms because the switching frequency is close to their resonant frequency [26]. Therefore, these variables can be analyzed using the fundamental harmonic approximation (FHA). By employing the EDF method in papers [23], [26], [34], [35], and [36], these variables can be approximated as the sum of sinusoidal and cosine terms

$$x = x_s \sin(\omega_s t) + x_c \cos(\omega_s t) \tag{6}$$

where ω_s is the switching angular frequency, x can be i_{f1}, i_{f2}, i_f, i_{p1}, i_{p2}, i_s, v_{f1}, v_{f2}, v_{p1}, v_{p2}, and v_s.

The derivative of x is

$$x' = (x'_s - \omega_s x_c)\sin(\omega_s t) + (x'_c + \omega_s x_s)\cos(\omega_s t). \tag{7}$$

The resonant network is tuned to a frequency that permits only the fundamental frequency while suppressing all higher harmonics. Therefore, the nearly square waveforms of v_1 and v_2 can be approximated using the FHA concept by neglecting the higher harmonics, and represented by their fundamental components as follows [34]:

$$v_1 = \frac{4}{\pi} V_{\text{in}} \sin(\omega_s t) \triangleq V_e \sin(\omega_s t) \tag{8}$$

$$\begin{aligned} v_2 &= \text{sgn}(i_s)\left(v_{Cr} + 2V_F\right) \\ &= \frac{4}{\pi}\frac{i_{ss}\left(v_{Cr} + 2V_F\right)}{i_{\text{speak}}} \sin(\omega_s t) \\ &\quad + \frac{4}{\pi}\frac{i_{sc}\left(v_{Cr} + 2V_F\right)}{i_{\text{speak}}} \cos(\omega_s t) \end{aligned} \tag{9}$$

where i_{speak} is the peak value of i_s

$$i_{\text{speak}} = \sqrt{i_{ss}^2 + i_{sc}^2}. \tag{10}$$

By substituting (6)–(10) into the nonlinear state-space model obtained in the previous section, and noting that the coefficients of the sine and cosine terms on both sides of the equations are equal due to harmonic balance, a new set of equations is obtained

$$\begin{cases} i'_{f1s} = \left[V_e - v_{f1s} - 2R_{ds}\left(i_{f1s} + i_{f2s}\right)\right]/L_f + \omega_s i_{f1c} \\ i'_{f1c} = \left[-v_{f1c} - 2R_{ds}\left(i_{f1c} + i_{f2c}\right)\right]/L_f - \omega_s i_{f1s} \\ i'_{f2s} = \left[V_e - v_{f2s} - 2R_{ds}\left(i_{f1s} + i_{f2s}\right)\right]/L_f + \omega_s i_{f2c} \\ i'_{f2c} = \left[-v_{f2c} - 2R_{ds}\left(i_{f1c} + i_{f2c}\right)\right]/L_f - \omega_s i_{f2s} \\ i'_{p1s} = \left[\left(1 - k_2^2\right) L_s v_{\text{eq}1s} + \left(k_1 k_2 - k_p\right) L_s v_{\text{eq}2s} \right. \\ \qquad \left. + \left(k_1 - k_2 k_p\right)\sqrt{L_p L_s} v_{\text{eq}0s}\right]/L_{\text{eq}m} + \omega_s i_{p1c} \\ i'_{p1c} = \left[\left(1 - k_2^2\right) L_s v_{\text{eq}1c} + \left(k_1 k_2 - k_p\right) L_s v_{\text{eq}2c} \right. \\ \qquad \left. + \left(k_1 - k_2 k_p\right)\sqrt{L_p L_s} v_{\text{eq}0c}\right]/L_{\text{eq}m} - \omega_s i_{p1s} \end{cases} \tag{11}$$

$$\begin{cases} i'_{p2s} = \left[\left(1 - k_1^2\right) L_s v_{\text{eq}2s} + \left(k_1 k_2 - k_p\right) L_s v_{\text{eq}1s} \right. \\ \qquad \left. + \left(k_2 - k_1 k_p\right)\sqrt{L_p L_s} v_{\text{eq}0s}\right]/L_{\text{eq}m} + \omega_s i_{p2_c} \\ i'_{p2c} = \left[\left(1 - k_1^2\right) L_s v_{\text{eq}2c} + \left(k_1 k_2 - k_p\right) L_s v_{\text{eq}1c} \right. \\ \qquad \left. + \left(k_2 - k_1 k_p\right)\sqrt{L_p L_s} v_{\text{eq}0c}\right]/L_{\text{eq}m} - \omega_s i_{p2_s} \\ i'_{ss} = \left\{\sqrt{L_p L_s}\left[\left(k_1 - k_2 k_p\right) v_{\text{eq}1s} + \left(k_2 - k_1 k_p\right) v_{\text{eq}2s}\right] \right. \\ \qquad \left. + \left(1 - k_p^2\right) L_p v_{\text{eq}0s}\right\}/L_{\text{eq}m} + \omega_s i_{sc} \\ i'_{sc} = \left\{\sqrt{L_p L_s}\left[\left(k_1 - k_2 k_p\right) v_{\text{eq}1c} + \left(k_2 - k_1 k_p\right) v_{\text{eq}2c}\right] \right. \\ \qquad \left. + \left(1 - k_p^2\right) L_p v_{\text{eq}0c}\right\}/L_{\text{eq}m} - \omega_s i_{ss} \end{cases} \tag{12}$$

$$\begin{cases} v'_{f1s} = \left(i_{f1s} - i_{p1s}\right)/C_f + \omega_s v_{f1c} \\ v'_{f1c} = \left(i_{f1c} - i_{p1c}\right)/C_f - \omega_s v_{f1_s} \\ v'_{f2s} = \left(i_{f2s} - i_{p2s}\right)/C_f + \omega_s v_{f2_c} \\ v'_{f2c} = \left(i_{f2c} - i_{p2c}\right)/C_f - \omega_s v_{f2_s} \\ v'_{p1s} = i_{p1s}/C_p + \omega_s v_{p1_c} \\ v'_{p1c} = i_{p1c}/C_p - \omega_s v_{p1_s} \\ v'_{p2s} = i_{p2s}/C_p + \omega_s v_{p2_c} \\ v'_{p2c} = i_{p2c}/C_p - \omega_s v_{p2_s} \\ v'_{ss} = i_{ss}/C_s + \omega_s v_{sc} \\ v'_{sc} = i_{sc}/C_s - \omega_s v_{ss} \\ v'_{Cr} = 2i_{\text{speak}}/\left(\pi C_r\right) - v_{Cr}/\left(C_r R_L\right) \end{cases}. \tag{13}$$

The nonlinear (11)–(13) constitute the simplified state equations of the DWPT system. At this point, the state variables are redefined as follows:

$$\begin{aligned} \mathbf{x} = [&i_{f1s}\ i_{f1c}\ \ i_{f2s}\ i_{f2c}\ i_{p1s}\ i_{p1c}\ i_{p2s}\ i_{p2c}\ i_{ss}\ i_{sc} \\ &v_{f1s}\ v_{f1c}\ v_{f2s}\ v_{f2c}\ v_{p1s}\ v_{p1c}\ v_{p2s}\ v_{p2c}\ v_{ss}\ v_{sc}\ v_{Cr}]^T. \end{aligned} \tag{14}$$

C. Steady-State Model and Linearized Small-Signal Model

During the motion process of DWPT, a small-signal model can be derived by introducing a small perturbation $\hat{\mathbf{k}}$ around the steady-state coupling coefficient $\mathbf{K}$. The perturbation $\hat{\mathbf{k}}$will cause each state variable to change, represented as its steady-state value and its small-signal component:

$$\mathbf{x} = \mathbf{X} + \hat{\mathbf{x}}. \tag{15}$$

To obtain the linearized small-signal model, the nonlinear terms in (12) and (13) need to be linearized around a specific steady-state operating point. By applying Taylor's Theorem

and retaining the steady-state values and the first-order Taylor polynomial, the linearized model can be derived

$$\begin{cases} 1/L_{eqm} \approx -1/K_{eqm}L_pL_s - 2\left[(K_1-K_2K_p)\hat{k}_1 \right. \\ \left. +(K_2-K_1K_p)\hat{k}_2+(K_P-K_1K_2)\hat{k}_p\right]\Big/ K_{eqm}{}^2L_pL_s \\ i_{fpeak}\approx I_{fpeak}+\left[I_{fs}\left(\hat{i}_{f1s}+\hat{i}_{f2s}\right)+I_{fc}\left(\hat{i}_{f1c}+\hat{i}_{f2c}\right)\right]\Big/ I_{fpeak} \\ i_{ss}\left(v_{cr}+2V_F\right)/i_{speak} \approx I_{ss}\left(V_{cr}+2V_F+\hat{v}_{cr}\right)/I_{speak} \\ +(V_{cr}+2V_F)\left(I_{sc}^2\hat{i}_{ss}-I_{ss}I_{sc}\hat{i}_{sc}\right)\Big/ I_{speak}^3 \\ i_{sc}\left(v_{cr}+2V_F\right)/i_{speak} \approx I_{sc}\left(V_{cr}+2V_F+\hat{v}_{cr}\right)/I_{speak} \\ +(V_{cr}+2V_F)\left(I_{ss}^2\hat{i}_{sc}-I_{ss}I_{sc}\hat{i}_{ss}\right)\Big/ I_{speak}^3 \end{cases} \tag{16}$$

where

$$K_{eqm} = 1 - K_1^2 - K_2^2 + 2K_1K_2K_p - K_p^2. \tag{17}$$

By substituting (15)–(17) into (12) and (13), then separating the steady-state components from the small-signal components, the linearized small-signal model is obtained in the matrix form (18). The steady-state values in **A**, **B**, and **C** can be solved through the separated steady-state component equations

$$\frac{\mathrm{d}}{\mathrm{dt}}\hat{\mathbf{x}} = \mathbf{A}\hat{\mathbf{x}} + \mathbf{B}\hat{\mathbf{k}}. \tag{18}$$

Since we mainly focus on the primary side inverter output current i_f and the secondary-side rectifier output voltage v_{out}, the system's output equations can be represented in the following matrix form:

$$\hat{\mathbf{y}} = \begin{bmatrix} \hat{\mathrm{i}}_{f\mathrm{peak}} \\ \hat{\mathrm{v}}_{\mathrm{out}} \end{bmatrix} = \mathbf{C}\hat{\mathbf{x}}. \tag{19}$$

The coefficient matrices **A**, **B**, and **C** are provided in the Appendix. At this point, the state variables are transformed into their small-signal components, denoted as $\hat{\mathbf{x}}$, expressed as follows:

$$\hat{\mathbf{x}} = \left[\hat{i}_{f1s}\,\hat{i}_{f1c}\,\hat{i}_{f2s}\,\hat{i}_{f2c}\,\hat{i}_{p1s}\,\hat{i}_{p1c}\,\hat{i}_{p2s}\,\hat{i}_{p2c}\,\hat{i}_{ss}\,\hat{i}_{sc}\right.$$
$$\left.\hat{v}_{f1s}\,\hat{v}_{f1c}\,\hat{v}_{f2s}\,\hat{v}_{f2c}\,\hat{v}_{p1s}\,\hat{v}_{p1c}\,\hat{v}_{p2s}\,\hat{v}_{p2c}\,\hat{v}_{ss}\,\hat{v}_{sc}\,\hat{v}_{Cr}\right]^T. \tag{20}$$

Similarly, the input variables are transformed into their small-signal components, denoted as $\hat{\mathbf{k}}$, expressed as follows:

$$\hat{\mathbf{k}} = \begin{bmatrix} \hat{k}_1 & \hat{k}_2 & \hat{k}_p \end{bmatrix}^T. \tag{21}$$

By transforming (18) and (19) into the s-domain, the transfer functions from $\hat{\mathbf{k}}$ to $\hat{i}_{f\mathrm{peak}}$ and $\hat{v}_{out}$ can be obtained, which are expressed as follows:

$$\begin{cases} \mathbf{G_{ifk}}(\mathbf{s}) \triangleq \frac{\hat{i}_{f\mathrm{peak}}(s)}{\hat{\mathbf{k}}(\mathbf{s})} = \begin{bmatrix} 1 & 0 \end{bmatrix}\mathbf{C}(s\mathbf{I}-\mathbf{A})^{-1}\mathbf{B} \\ \mathbf{G_{vk}}(\mathbf{s}) \triangleq \frac{\hat{v}_{\mathrm{out}}(s)}{\hat{\mathbf{k}}(\mathbf{s})} = \begin{bmatrix} 0 & 1 \end{bmatrix}\mathbf{C}(s\mathbf{I}-\mathbf{A})^{-1}\mathbf{B} \end{cases}. \tag{22}$$

Where $\mathbf{G_{vk}(s)}$ comprises the transfer functions $G_{vk1}(\mathrm{s})$, $G_{vk2}(\mathrm{s})$, and $G_{vkp}(\mathrm{s})$, which correspond to k_1, k_2, and k_p to v_{out}, respectively. Similarly, $\mathbf{G_{ifk}(s)}$ includes the transfer functions $G_{ifk1}(\mathrm{s})$, $G_{ifk2}(\mathrm{s})$, and $G_{ifkp}(\mathrm{s})$. Overall, the modeling process introduced in this section is illustrated in Fig. 4.

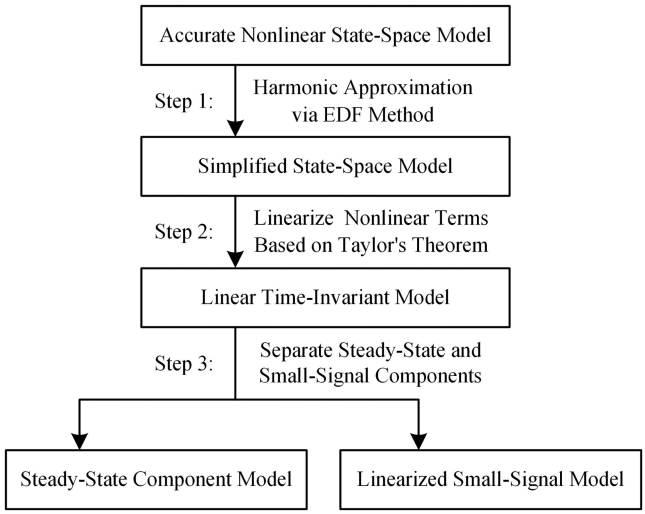

Fig. 4. Flowchart of the modeling process.

TABLE I
PARAMETERS OF THE LCC-S DWPT SYSTEM

Parameters	Values	Parameters	Values
V_{in}	100 V	f_s	140 kHz
R_{ds}	0.02 Ω	L_s	49.1 μH
V_F	0.2 V	C_s	26.3 nF
L_f	21.6 μH	R_p	0.17 Ω
C_f	59.5 nF	R_s	0.15 Ω
L_p	51.2 μH	R_L	8 Ω
C_p	53.4 nF		

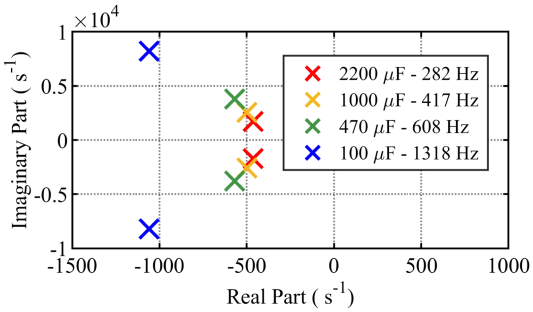

Fig. 5. Dominant pole plot of DWPT small-signal model.

III. Transient Model Response and Bode Plot Analysis

A. Transient Response Under Different Motion Speeds

In the linearized small-signal model presented in Section II, the poles of $\mathbf{G_{ifk}(s)}$ and $\mathbf{G_{vk}(s)}$ correspond to the eigenvalues of matrix **A**. Using the system parameters from Table I, the dominant pole plot of the small-signal model is illustrated in Fig. 5. As the output capacitance C_{r} decreases, the dominant modal frequency increases correspondingly. To investigate the system's response characteristics, it is crucial to determine the frequency range of the input signal.

Fig. 6 shows the spatial distribution and dimensions of the experimental coils. The transmitter coils each measure 146 mm on a side, and the receiver coil measures 140 mm on a side,

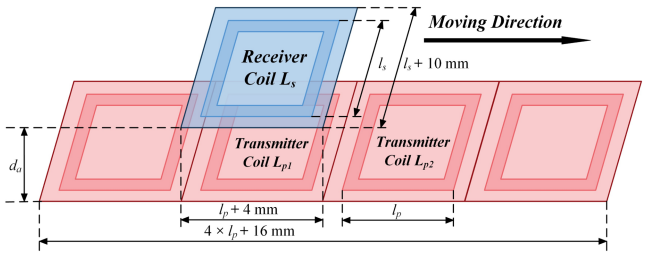

Fig. 6. Spatial distribution and size of experimental coils.

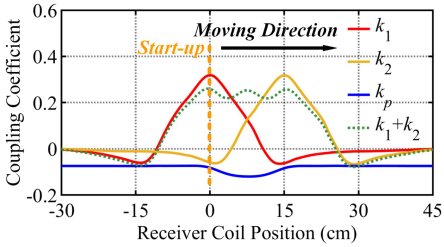

Fig. 7. Coupling coefficient versus receiver coil position plot.

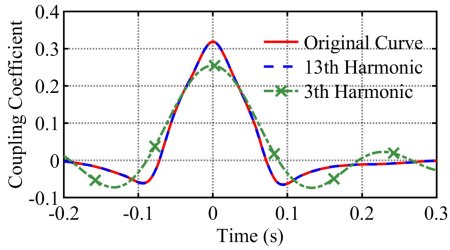

Fig. 8. Fourier-based curve fitting of k_1 versus time: 13th-order harmonic versus 3rd-order harmonic approximations.

with a vertical distance of 25 mm between them. As described in Section II, the DWPT system features a modular and periodic design, where the receiver coil primarily interacts with two adjacent transmitter coils during each motion cycle. Consequently, in the small-signal modeling and experimental setup, the transmitter coils at both ends are deliberately disconnected to avoid edge effects, and only the two middle coils are connected to the circuit to represent the typical coupling scenario. This configuration effectively captures the dominant electromagnetic interactions while simplifying the boundary conditions, ensuring the modeling results remain representative of the actual DWPT operating environment. Fig. 7 presents the relationship between the coupling coefficient **k** and the receiver's position, where the position is defined as zero when the receiving coil is directly above the transmitting coil L_{p1}. By dividing the position by a specified speed, it is possible to obtain the relationship between **k** and time. This relationship can then be decomposed by applying the Fourier decomposition as follows:

$$\hat{\mathbf{k}}(\mathbf{t}) \approx \mathbf{a_0} + \sum_{n=1}^{N} \left(\mathbf{c_n} \cos\left(2\pi n \cdot f_k t\right)\right). \tag{23}$$

In (23), when the transport system reaches its maximum operating speed v of 1.5 m/s, the frequency of the input signal also attains its maximum. Under these conditions, the integer N takes the value 31, and the fundamental frequency f_k of **k** is 1.59 Hz. In practice, as shown in Fig. 8, the curve obtained by summing the DC component and the first 13 harmonic components while discarding higher order terms perfectly matches the original curve. Therefore, the primary focus lies on the low-frequency characteristics of $\mathbf{G_{ifk}(s)}$ and $\mathbf{G_{vk}(s)}$ below the 13th harmonic, corresponding to 20.6 Hz. From Fig. 5, we can see that 20.6 Hz is much lower than the system's lowest dominant modal frequency, 282 Hz. Therefore, in this article, the input signal frequency is significantly lower than the system's dominant modal frequency. This results in a rapid decay of high-frequency dynamics, including brief transient responses. Consequently, the remaining response predominantly exhibits steady-state behavior, meaning the overall system response closely approximates its steady-state response. Therefore, by leveraging this low-frequency approximation, Bode plots can be used to analyze and predict the system's response to variations in the coupling coefficient. Figs. 9 and 10 present the Bode amplitude plots of $\mathbf{G_{ifk}(s)}$ and $\mathbf{G_{vk}(s)}$ under different rectifier output capacitances C_r.

According to (23), the system input frequency f_k increases with rising motion speed. Referring to the Bode plot of $\mathbf{G_{ifk}(s)}$ in Fig. 9, one observes that, in the low-frequency range, the amplitude increases with frequency. This implies that as the speed grows, the current $i_{f\text{peak}}$ is expected to experience stronger fluctuations. However, the Bode plot of $\mathbf{G_{vk}(s)}$ shows that in the low-frequency range, the magnitude remains at 47.01 or –2.36 dB. Since the frequency after the speed change still falls within this low-frequency range, the waveform of v_{out} remains unaffected.

By applying the Laplace transform, we obtain the frequency-domain expression of the input

$$\hat{\mathbf{k}}(\mathbf{s}) = \mathcal{L}\left\{\hat{\mathbf{k}}(\mathbf{t})\right\} = \frac{\mathbf{a_0}}{s} + \sum_{n=1}^{N}\left(\mathbf{c_n} \cdot \frac{s}{s^2 + (2\pi n \cdot f_k)^2}\right). \tag{24}$$

Then, by multiplying (24) by (22) and performing the inverse Laplace transform, the time-domain responses are derived:

$$\begin{cases} i_{f\text{peak}}(t) = \mathcal{L}^{-1}\left\{\hat{\mathbf{k}}(\mathbf{s}) \cdot \mathbf{G_{ifk}}(\mathbf{s})\right\} \\ v_{\text{out}}(t) = \mathcal{L}^{-1}\left\{\hat{\mathbf{k}}(\mathbf{s}) \cdot \mathbf{G_{vk}}(\mathbf{s})\right\} \end{cases}. \tag{25}$$

Fig. 11(a) shows the small-signal model response of $i_{f\text{peak}}$ when the receiver coil moves at speeds of 1.5, 1, and 0.5 m/s, with the output capacitance fixed at 2200 μF. As predicted by the Bode plot analysis in Fig. 10, the $i_{f\text{peak}}$ exhibits progressively greater fluctuation amplitude at higher speeds. In particular, the 1.5 m/s curve exhibits the largest magnitude oscillations, while the 0.5 m/s case remains relatively mild. Fig. 11(b) depicts the corresponding small-signal response of v_{out} under these different speeds. Consistent with the Bode plot prediction, the v_{out} waveform is virtually unaffected by changes in the receiver coil's motion speed. Hence, the small-signal model results confirm

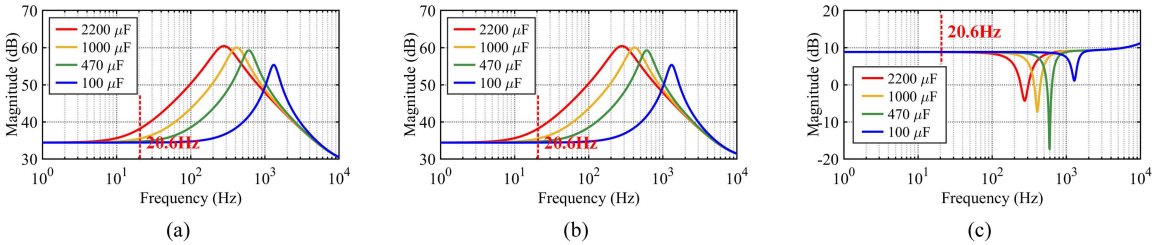

Fig. 9. Bode amplitude plots of $\mathbf{G_{ifk}(s)}$ for inverter output current $i_{f\mathrm{peak}}$ under different output filter capacitances C_r. (a) G_{ifk1}(s); (b) G_{ifk2}(s); (c) G_{ifkp}(s).

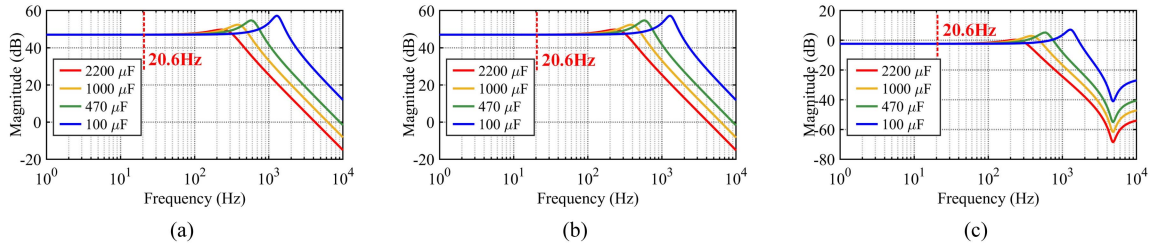

Fig. 10. Bode amplitude plots of $\mathbf{G_{vk}(s)}$ for rectifier output voltage v_{out} under different output filter capacitances C_r. (a) G_{vk1}(s); (b) G_{vk2}(s); (c) G_{vkp}(s).

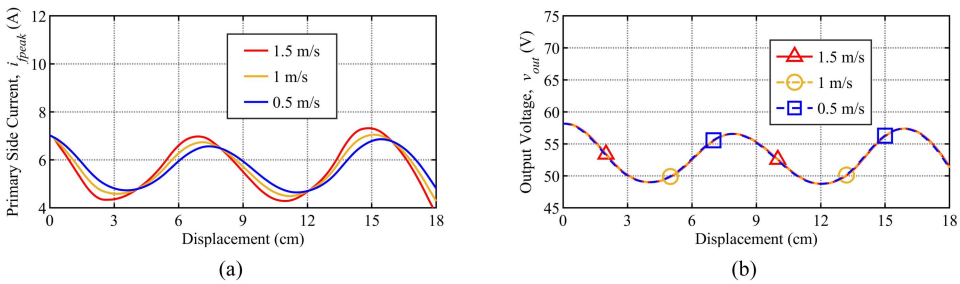

Fig. 11. Small-signal transient response for different motion speeds v. (a) Primary side inverter output current $i_{f\mathrm{peak}}$. (b) Rectifier output voltage v_{out}.

that $i_{f\mathrm{peak}}$ grows in the fluctuation amplitude at higher motion speeds, whereas v_{out} remains stable and largely invariant with respect to motion speed variations.

B. Transient Response Under Different Output Capacitances

Referring to the Bode plot of $\mathbf{G_{ifk}(s)}$ in Fig. 9, changes in the output capacitance C_r alter the system's amplitude frequency response characteristics. Larger capacitance values prompt the amplitude responses in the low-frequency region to reach higher peaks, but they also lead to more rapid attenuation at high frequencies. Since our primary focus lies in the low-frequency range, we can employ the Bode plot in this region to predict the behavior of $i_{f\mathrm{peak}}$. Compared to smaller capacitances, larger ones exhibit greater oscillation in the response magnitude.

Fig. 12(a) shows the small-signal model response of the primary side inverter output current $i_{f\mathrm{peak}}$ under different output capacitances at a motion speed of 1.5 m/s. It is apparent that the capacitance value significantly influences the response of $i_{f\mathrm{peak}}$. The greater the capacitance value, the more pronounced the fluctuation in the response curve, indicating that $i_{f\mathrm{peak}}$ becomes more sensitive to variations in the input signal. In contrast, smaller capacitances effectively smooth out these fluctuations.

Meanwhile, the Bode plot of $\mathbf{G_{vk}(s)}$ indicates that increasing the capacitance value causes an earlier magnitude drop at high frequencies. Nevertheless, in the low-frequency domain, which is our main region of interest, different capacitances exhibit similar response characteristics. Hence, it can be inferred that variations in C_r do not significantly affect the behavior of v_{out}. Fig. 12(b) compares the output voltage v_{out} responses under different capacitance values and confirms that the voltage waveforms are nearly identical. As predicted by the Bode plot analysis, changing the output filter capacitance C_r has minimal influence on v_{out}.

C. Transient Response Under Different Start-Up Accelerations

In linear transportation systems, frequent starts and stops make it essential to investigate the transient response during the start-up phase. The primary distinction in transient behavior

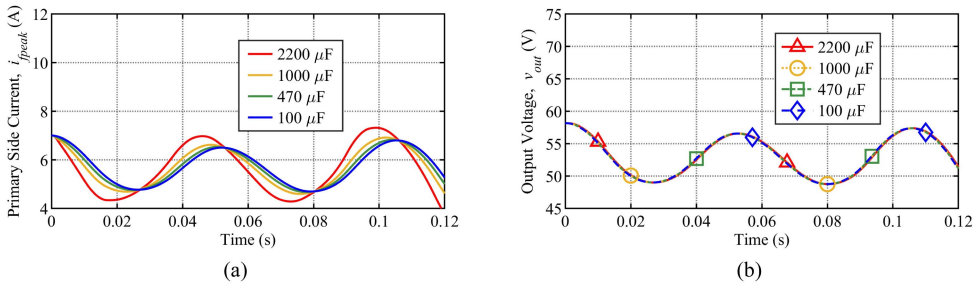

Fig. 12. Small-signal transient response for different output capacitances C_r. (a) Primary side inverter output current $i_{f\text{peak}}$. (b) Rectifier output voltage v_{out}.

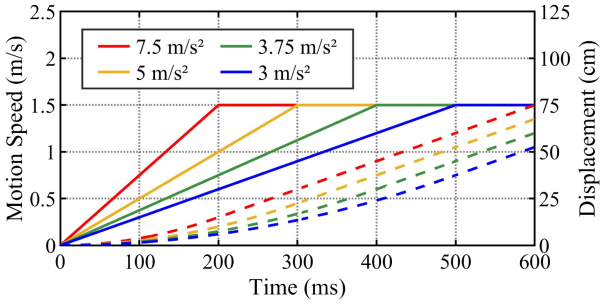

Fig. 13. Motion speed and displacement curves for different start-up accelerations during the ramp-up phase to 1.5 m/s.

arises from differences in acceleration during linear ramp-up. Hence, four start-up accelerations of 7.5, 5, 3.75, and 3 m/s^2 are chosen for comparative analysis, corresponding to linear acceleration times of 200, 300, 400, and 500 ms, respectively. Fig. 13 depicts the velocity and displacement curves for these start-up accelerations as they ramp up to 1.5 m/s. At the onset of motion, the system remains in a low-speed state, meaning the input frequency does not exceed 10 Hz. Taking the Bode plot of $i_{f\text{peak}}$ under a 2200 μF output capacitance as an example, the response shows limited variation below 10 Hz. Therefore, in the initial start-up interval, the fluctuation amplitude of $i_{f\text{peak}}$ should be similar for all tested accelerations. However, as time progresses, the system with a higher start-up acceleration reaches a higher input frequency earlier. Beyond 10 Hz in the Bode plot, a noticeable increase in the response curve occurs, implying that, as the system advances, the difference in fluctuation amplitude across different start-up accelerations becomes increasingly pronounced.

Fig. 14(a) shows the small-signal model response of $i_{f\text{peak}}$ under these different start-up accelerations. Two sets of troughs and peaks can be observed. While the four systems exhibit similar oscillation magnitudes during the first set of troughs and peaks, distinct differences appear in the second set. Consistent with the Bode-plot-based analysis, faster start-up accelerations lead to progressively larger fluctuations as the system continues to accelerate.

Throughout the entire motion, the Bode plot for v_{out} at the corresponding frequencies remains unchanged. Below 50 Hz, the magnitude remains close to 47.01 dB. Hence, the oscillation amplitude of v_{out} is identical across different accelerations. This outcome is confirmed by the time-domain responses of v_{out} in Fig. 14(b), where only a slight delay is introduced by the change in acceleration, without altering the magnitude of v_{out} fluctuations.

D. Transient Response Under Different Input Voltages

Figs. 15 and 16 present the Bode magnitude plots of the system transfer functions $\mathbf{G_{ifk}(s)}$ and $\mathbf{G_{vk}(s)}$ under different input voltages V_{in}. As observed, increasing V_{in} leads to an upward shift in the magnitude curves of both $\mathbf{G_{ifk}(s)}$ and $\mathbf{G_{vk}(s)}$ across the entire frequency spectrum. This indicates that higher input voltages result in stronger peak responses, suggesting that larger V_{in} values are likely to induce more pronounced fluctuations in both the primary-side inverter current $i_{f\text{peak}}$ and the output voltage v_{out}.

Based on (25), the transient small-signal responses of $i_{f\text{peak}}$ and v_{out} under different input voltages were obtained for the conditions of 1.5 m/s motion speed and 2200 μF output capacitance. To facilitate a direct comparison of the variation in fluctuation amplitudes, the initial value at $t = 0$ was subtracted from each response curve, as shown in Fig. 17. The results indicate that with increasing V_{in}, the fluctuation amplitudes of both $i_{f\text{peak}}$ and v_{out} increase proportionally. Unlike the previously studied parameters, to which v_{out} was relatively insensitive, v_{out} as well as $i_{f\text{peak}}$ are both significantly affected by variations in the input voltage V_{in}.

E. Transient Response Under Different Load Resistances

As shown in the Bode magnitude plot of $\mathbf{G_{ifk}(s)}$ in Fig. 18, variations in the load resistance R_L affect the system's amplitude response characteristics. Smaller loads exhibit higher magnitude responses in the low-frequency region, leading to stronger peak responses. However, in the high-frequency region, the magnitude curves corresponding to different loads are nearly identical. Since the primary focus of this article is the low-frequency range, the Bode plot suggests that smaller loads are expected to induce greater fluctuations in the inverter output current $i_{f\text{peak}}$. On the other hand, the Bode plot of $\mathbf{G_{vk}(s)}$ in Fig. 19 shows that the magnitude curves remain almost unchanged across all frequencies regardless of the load. This implies that load variation has a negligible impact on v_{out} fluctuation, which is consistent with the constant voltage characteristic of the LCC-S topology.

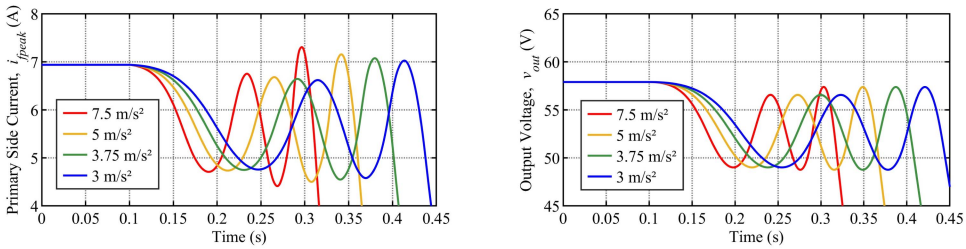

Fig. 14. Small-signal transient response for different start-up accelerations a_0. (a) Primary side inverter output current $i_{f\mathrm{peak}}$. (b) Rectifier output voltage v_{out}.

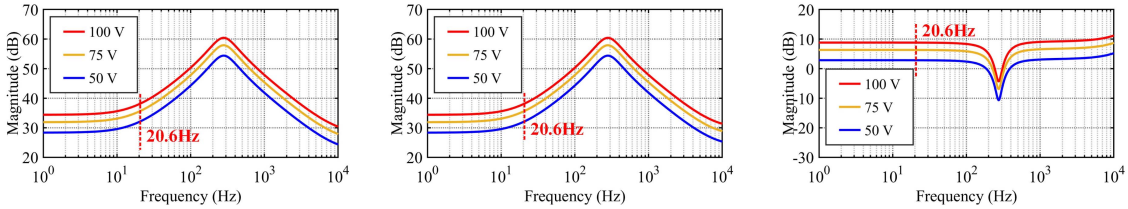

Fig. 15. Bode amplitude plots of $\mathbf{G_{ifk}(s)}$ for inverter output current $i_{f\mathrm{peak}}$ under different input voltages V_{in}. (a) $G_{ifk1}(s)$. (b) $G_{ifk2}(s)$. (c) $G_{ifkp}(s)$.

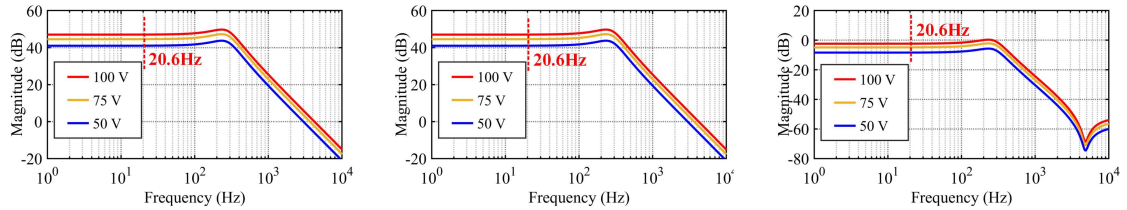

Fig. 16. Bode amplitude plots of $\mathbf{G_{vk}(s)}$ for rectifier output voltage v_{out} under different input voltages V_{in}. (a) $G_{vk1}(s)$; (b) $G_{vk2}(s)$; (c) $G_{vkp}(s)$.

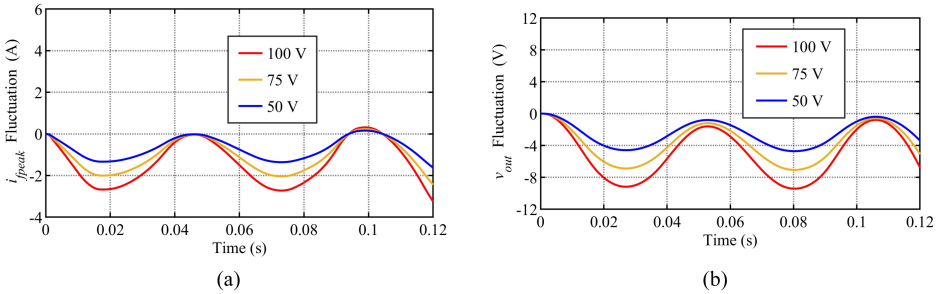

Fig. 17. Normalized small-signal transient response for different input voltages V_{in}. (a) Inverter output current $i_{f\mathrm{peak}}$. (b) Rectifier output voltage v_{out}.

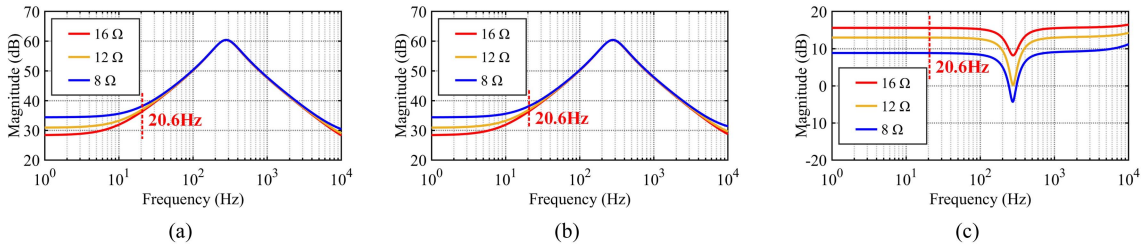

Fig. 18. Bode amplitude plots of $\mathbf{G_{ifk}(s)}$ for inverter output current $i_{f\mathrm{peak}}$ under different input voltages V_{in}. (a) $G_{ifk1}(s)$. (b) $G_{ifk2}(s)$. (c) $G_{ifkp}(s)$.

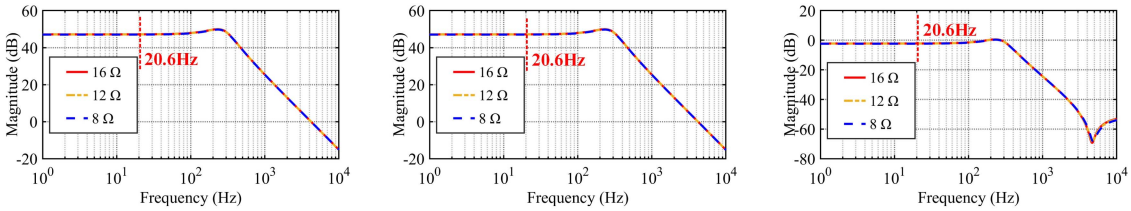

Fig. 19. Bode amplitude plots of $\mathbf{G_{vk}(s)}$ for rectifier output voltage $v_{\rm out}$ under different input voltages $V_{\rm in}$. (a) G_{vk1}(s). (b) G_{vk2}(s). (c) G_{vkp}(s).

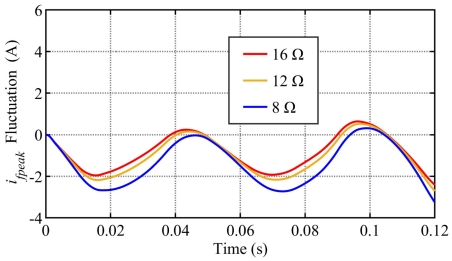

Fig. 20. Normalized small-signal transient response of inverter output current $i_{f\rm peak}$ for different load resistances R_L.

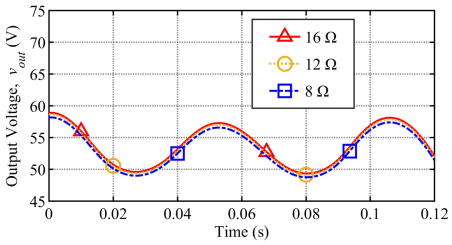

Fig. 21. Small-signal transient response of rectifier output voltage $v_{\rm out}$ for different load resistances R_L.

To clearly compare the fluctuation characteristics of $i_{f\rm peak}$ under different load conditions, each transient small-signal response curve of $i_{f\rm peak}$ was processed by subtracting its initial value at $t = 0$, as shown in Fig. 20. The results clearly demonstrate that as the load R_L decreases, the fluctuation amplitude of $i_{f\rm peak}$ significantly increases, which is consistent with the prediction presented earlier. Fig. 21 displays the corresponding transient responses of $v_{\rm out}$ under different loads. The voltage waveforms are nearly identical, confirming the Bode plot prediction that variations in R_L have little to no effect on the output voltage waveform.

IV. Experimental Verification

In this section, the LCC-S DWPT system model derived earlier is experimentally validated. A DWPT experimental platform was developed, as shown in Fig. 22, and the parameters of the LCC-S DWPT system are listed in Table I. The receiver coil is placed on a sliding track with controllable speed and start-up acceleration, thereby simulating the DWPT motion process. The receiver coil moves laterally along the track and thus does not experience any vertical misalignment, so the experiment focuses on the lateral displacement of the receiver coil. The variation of the coupling coefficient $\mathbf{k}$ with the receiver coil's position is depicted in Fig. 7. As discussed in Section II, the DWPT system exhibits modularity and periodicity. Hence, the motion from one transmitter coil to the next is selected to validate the small-signal model.

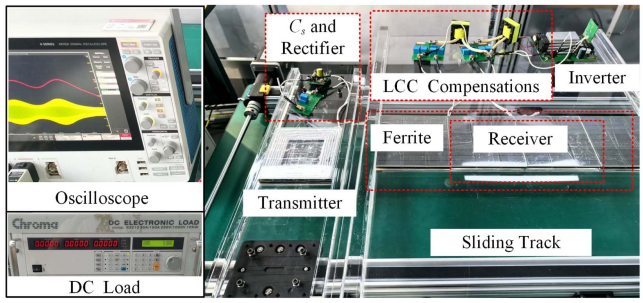

Fig. 22. Photograph of the DWPT experimental platform with controllable speed and start-up acceleration.

Fig. 23. Screenshot from power analyzer measurement.

In industrial manufacturing, the power supply demand for movers in linear transport and magnetically levitated transport systems typically ranges from tens of watts to approximately 100 W. To better reflect the broader application scenarios of DWPT systems, the experimental output power in this study was extended beyond the conventional 100 W level to 441.4 W. The screenshot of the power analyzer measurement is shown in Fig. 23, demonstrating that the system achieved the output efficiency of 91.85% at this elevated power level. The primary sources of loss originate from the coils and the rectifier. The

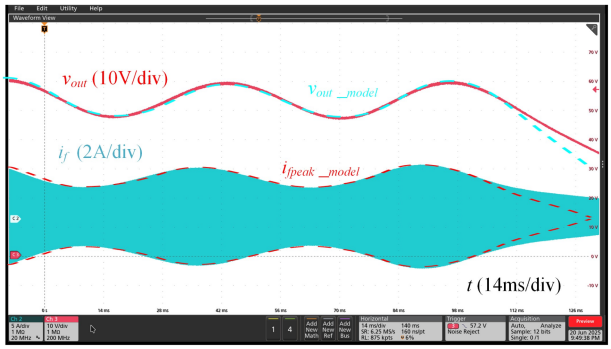

Fig. 24. Screenshot of experimental results at $C_r = 2200\ \mu$F and $v = 1.5$ m/s.

following discussion focuses on the system's response under various motion speeds, output filter capacitance values, start-up accelerations, input voltages, and load resistances.

A. Experiments of Different Motion Speeds

Initially, the receiver coil passes over the transmitter coils at different constant speeds with the output capacitance C_r fixed at 2200 μF. Leveraging the system's modularity and periodicity, we examine only the transition from one transmitter coil to the next. Fig. 24 shows the waveform screenshot of the response at a speed of 1.5 m/s. The red trace represents the measured output voltage v_{out}, while the dotted blue line indicates the corresponding value predicted by our reduced-order small-signal model. The blue trace represents the measured primary side current i_f, and the dotted red line shows the model's prediction for the peak of primary current $i_{f\text{peak}}$. We observe a close match between the red trace and the dotted blue line, indicating that our transient model accurately predicts the output voltage v_{out}. The dotted red line also provides a good envelope for the blue waveform. In the final stages, however, the large variation in the coupling coefficient moves the system farther from its steady-state operating point, thereby enhancing nonlinear characteristics and causing minor discrepancies between the measured and simulated responses. Overall, the transient model derived in this article can accurately predict the transient behavior of the DWPT system.

Fig. 25 contrasts the time-compressed experimental response results at different speeds, confirming consistency with the trends in Fig. 11. Using the first peak of the 0.5 m/s curve in Fig. 25(a) as a reference point, we compare the fluctuation amplitude of i_f for different motion speeds, as illustrated in Fig. 26(a). The fluctuation amplitude shows a linear relationship with the motion speed. As the motion speed increases from 0.5 to 1.5 m/s, the current fluctuation amplitude increases by approximately 0.41 A.

B. Experiments of Different Output Filter Capacitances

Next, we conducted experiments at 1.5 m/s with different output filter capacitances C_r. Fig. 27 compares the experimental responses under various capacitance values, and the resulting trends are consistent with those in Fig. 12. Taking the first peak of the 100 μF curve in Fig. 27(a) as a reference, we compare the fluctuation amplitude of i_f for different capacitance values in Fig. 26(b). The fluctuation amplitude exhibits an approximately linear correlation with the output capacitance size. As the output capacitance increases from 100 to 2200 μF, the current fluctuation amplitude increases by about 0.47 A.

C. Experiments of Different Start-Up Accelerations

Additionally, we investigate different start-up accelerations by placing the receiver coil at the center of the transmitter coil L_{p1}. Fig. 28 provides the experimental response results for different start-up accelerations a_0. Employing the 3 m/s^2 curve in Fig. 28(a) as a baseline, we quantify the fluctuation amplitude of i_f under different start-up accelerations, as shown in Fig. 26(c). The fluctuation amplitude exhibits a linear dependence on speed, and the disparity between the second trough-peak set is notably larger than the first. At the initial valley, when the start-up acceleration increases from 3 to 7.5 m/s^2, the current fluctuation amplitude only increases by approximately 0.05 A. However, by the final peak, the current fluctuation amplitude increases by about 0.28 A. This demonstrates that as the receiving coil advances and the start-up acceleration increases, the fluctuation amplitude of the inverter output current i_f becomes more pronounced, consistent with the analysis in Section III.

D. Experiments of Different Input Voltages

Experiments were conducted under different input voltages V_{in}, with the receiver coil moving at a constant speed of 1.5 m/s and the output capacitance fixed at 2200 μF. To facilitate a direct comparison of fluctuation amplitudes, each transient small-signal response curve of i_f and v_{out} was processed by subtracting its initial value at $t = 0$, as shown in Fig. 29. The overall experimental trends align well with the simulation results presented in Fig. 16. The initial i_f values corresponding to 100, 75, and 50 V input voltages were 8.36, 5.75, and 3.92 A, respectively, while the initial v_{out} values were 60.0, 45.0, and 29.9 V. Using the first trough of the 50 V curve as a reference point, Fig. 30 compares the fluctuation amplitudes of i_f and v_{out} under different V_{in} conditions. The results demonstrate an approximately linear relationship: as V_{in} increases from 50 to 100 V, the fluctuation amplitude of i_f increases by about 1.34 A, while that of v_{out} increases by approximately 4.59 V.

E. Experiments Under Different Load Resistances

Experiments were conducted under varying load resistances R_L. To facilitate a direct comparison of i_f fluctuations, each experimental response curve of i_f was processed by subtracting its initial value at $t = 0$, as shown in Fig. 31. The initial i_f values corresponding to the 16, 12, and 8 Ω load conditions were 5.02, 6.08, and 8.36 A, respectively. From Fig. 31, it can be observed that as the load increases from to 16 Ω, the fluctuation amplitude of i_f decreases by approximately 0.72 A.

Fig. 32 also shows the experimental responses of v_{out} under different load conditions. Due to the internal resistance of the coils and other circuit components, the output voltage exhibits a slight increase with increasing load. Nevertheless, the overall

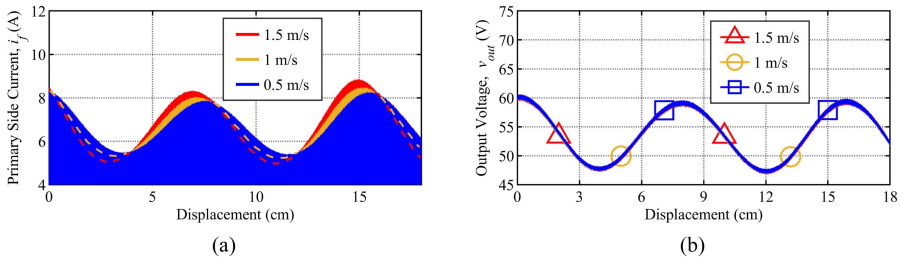

Fig. 25. Experimental response results for different motion speeds v. (a) Primary side inverter output current i_f. (b) Rectifier output voltage v_{out}.

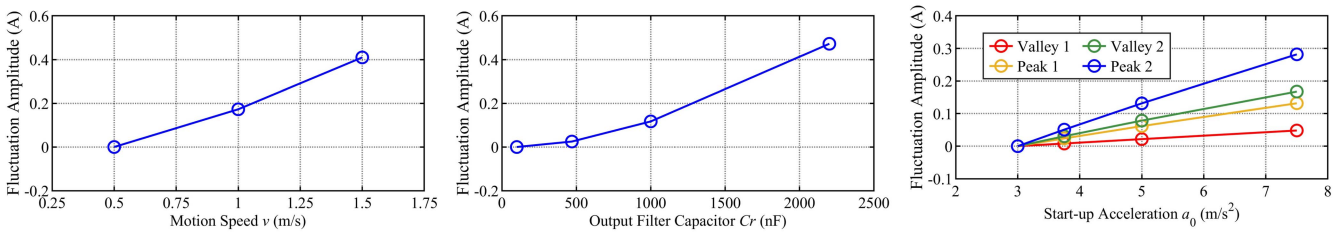

Fig. 26. Fluctuation amplitude of inverter output current i_f. (a) At different motion speeds. (b) At different output filter capacitances. (c) At different start-up accelerations.

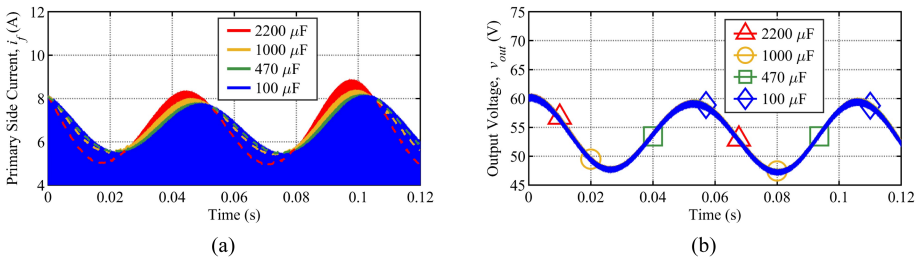

Fig. 27. Experimental response results for different output capacitances C_r. (a) Primary side inverter output current i_f. (b) Rectifier output voltage v_{out}.

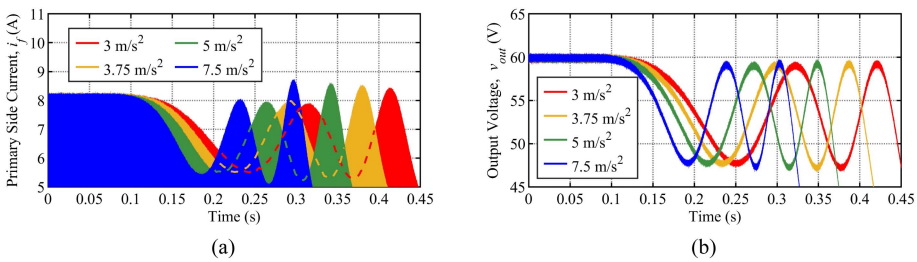

Fig. 28. Experimental response results for different start-up accelerations a_0. (a) Primary side inverter output current i_f. (b) Rectifier output voltage v_{out}.

behavior still reflects the constant-voltage characteristic of the LCC-S topology. In summary, the experimental results confirm that v_{out} fluctuations are largely insensitive to load variation, whereas i_f fluctuations decrease as the load increases, which is consistent with the analytical findings presented in Section III.

These findings confirm that the proposed transient model accurately predicts the DWPT system's transient behavior, thereby validating its correctness. Overall, v_{out} fluctuations are primarily influenced by input voltage, while remaining largely insensitive to variations in other parameters. By solving the steady-state components at different positions, the v_{out} response closely matches its theoretical steady-state value, which is determined by the combined coupling coefficient k_1+k_2. As shown in Fig. 7, the v_{out} waveform aligns with the k_1+k_2 profile, indicating that stabilizing k_1+k_2 through optimized coil design is an effective means to mitigate voltage fluctuations [12], [37]. In addition,

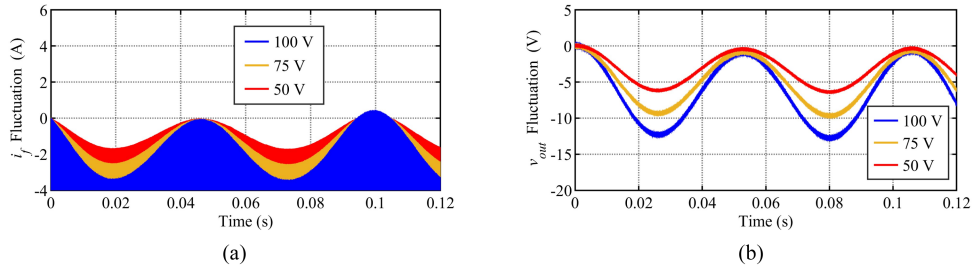

Fig. 29. Normalized experimental response results for different input voltages V_{in}. (a) Primary side inverter output current i_f. (b) Rectifier output voltage v_{out}.

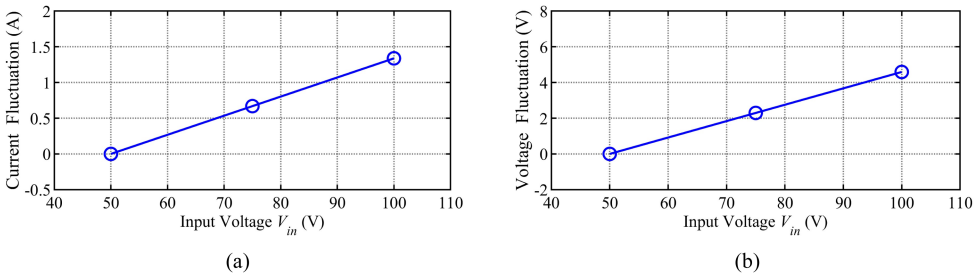

Fig. 30. Fluctuation amplitude for different input voltages V_{in}. (a) Primary side inverter output current i_f. (b) Rectifier output voltage v_{out}.

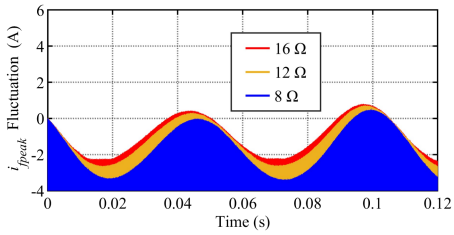

Fig. 31. Normalized experimental response results of primary side inverter output current i_f for different load resistances R_L.

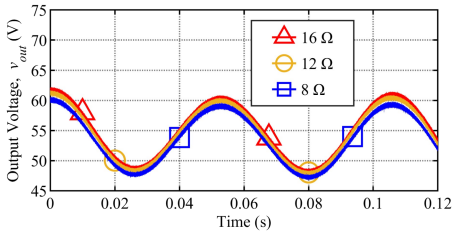

Fig. 32. Experimental response results of rectifier output voltage v_{out} for different load resistances R_L.

appropriate control and measurement strategies may also help suppress output voltage fluctuations [15], [16], [17], [18], [19]. In contrast, the fluctuation amplitude of i_f increases with larger output capacitance C_r, higher motion speed v, greater start-up acceleration a_0, elevated input voltage V_{in}, and reduced load resistance R_L. Therefore, appropriate adjustment of these parameters offers practical guidance for controlling current fluctuations and improving overall system dynamic performance.

V. Conclusion

This article developed a transient model for multitransmitter DWPT systems using the EDF method, which captures multicoupling effects by decomposing nonlinear coupling variations into sinusoidal inputs linked to motion speed. Our analysis shows that the dominant modal frequency is significantly higher than the coupling variation frequency, allowing the overall system response to closely approximate steady-state behavior. This finding enables a detailed parametric study that precisely quantifies the impacts of motion speed, output filter capacitance, start-up acceleration, input voltage, and load resistance on inverter current fluctuations and output voltage stability. Experimental results from a DWPT test platform validate the model's accuracy and confirm its practical value for enhancing system performance. Overall, our work provides a robust theoretical framework for analyzing and optimizing DWPT systems, paving the way for more effective control strategies.

Appendix

In this Appendix, we present the detailed expressions for the system matrices used in the small-signal state-space representation of the DWPT system. The state-space equations are given by the following:

$$\frac{d}{dt}\hat{\mathbf{x}} = \mathbf{A}\hat{\mathbf{x}} + \mathbf{B}\hat{\mathbf{k}}$$

$$\hat{\mathbf{y}} = \begin{bmatrix} \hat{i}_{f\text{peak}} \\ \hat{v}_{\text{out}} \end{bmatrix} = \mathbf{C}\hat{\mathbf{x}}$$

where $\mathbf{A} \in \mathbb{R}^{21\times 21}$, $\mathbf{B} \in \mathbb{R}^{21\times 3}$, and $\mathbf{C} \in \mathbb{R}^{2\times 21}$.

Due to the complexity of these matrices, they are first expressed in block form as follows:

$$\mathbf{A} = \begin{bmatrix} \mathbf{A_{i1}} & \mathbf{0_{4\times6}} & \mathbf{A_{v1}} & \mathbf{0_{4\times7}} \\ \mathbf{0_{6\times4}} & \mathbf{A_{i2}} & \mathbf{A_{v2}} & \\ & \mathbf{A_{i3}} & \mathbf{A_{v3}} & \end{bmatrix}$$

$$\mathbf{B} = \begin{bmatrix} & \mathbf{0_{4\times3}} & \\ \mathbf{B_1} & \mathbf{B_2} & \mathbf{B_3} \\ & \mathbf{0_{11\times3}} & \end{bmatrix}.$$

Given the intricacy of the repeated expressions within these blocks, we substitute lengthy terms with symbols X_1, X_2, …, X_{15}. The detailed expressions of these substitution symbols are provided as follows:

$$X_1 = K_{\text{eq}m} L_p$$
$$X_2 = K_{\text{eq}m} L_s$$
$$X_3 = K_{\text{eq}m} \sqrt{L_p L_s}$$
$$X_4 = K_1^2 - 1$$
$$X_5 = K_2^2 - 1$$
$$X_6 = K_p^2 - 1$$
$$X_7 = K_1 K_2 - K_p$$
$$X_8 = K_1 K_p - K_2$$
$$X_9 = K_2 K_p - K_1$$
$$X_{10} = \frac{4}{\pi} \frac{I_{ss} I_{sc} (V_{cr} + 2V_F)}{I_{\text{speak}}^3}$$
$$X_{11} = \frac{4}{\pi} \frac{I_{ss}^2 (V_{cr} + 2V_F)}{I_{\text{speak}}^3}$$
$$X_{12} = \frac{4}{\pi} \frac{I_{sc}^2 (V_{cr} + 2V_F)}{I_{\text{speak}}^3}$$
$$X_{13} = \frac{4}{\pi} \frac{I_{ss}}{I_{\text{speak}}}$$
$$X_{14} = \frac{4}{\pi} \frac{I_{sc}}{I_{\text{speak}}}$$
$$X_{15} = \frac{1}{K_{\text{eq}m} L_p L_s}.$$

Using these definitions, the block expressions for the matrices are then expressed in a concise form. Unnumbered equation shown as below:

$$\mathbf{A_{i1}} = \begin{bmatrix} -\frac{2R_{ds}}{L_f} & \omega_s & -\frac{2R_{ds}}{L_f} & 0 \\ -\omega_s & -\frac{2R_{ds}}{L_f} & 0 & -\frac{2R_{ds}}{L_f} \\ -\frac{2R_{ds}}{L_f} & 0 & -\frac{2R_{ds}}{L_f} & \omega_s \\ 0 & -\frac{2R_{ds}}{L_f} & -\omega_s & -\frac{2R_{ds}}{L_f} \end{bmatrix} \quad \mathbf{A_{i2}} = \begin{bmatrix} \frac{X_5}{X_1} R_p & \omega_s & -\frac{X_7}{X_1} R_p & 0 & \frac{X_9}{X_3} (R_s + X_{12}) & -\frac{X_9}{X_3} X_{10} \\ -\omega_s & \frac{X_5}{X_1} R_p & 0 & -\frac{X_7}{X_1} R_p & -\frac{X_9}{X_3} X_{10} & \frac{X_9}{X_3} (R_s + X_{11}) \\ -\frac{X_7}{X_1} R_p & 0 & \frac{X_4}{X_1} R_p & \omega_s & \frac{X_8}{X_3} (R_s + X_{12}) & -\frac{X_8}{X_3} X_{10} \\ 0 & -\frac{X_7}{X_1} R_p & -\omega_s & \frac{X_4}{X_1} R_p & -\frac{X_8}{X_3} X_{10} & \frac{X_8}{X_3} (R_s + X_{12}) \\ \frac{X_9}{X_3} R_p & 0 & \frac{X_8}{X_3} R_p & 0 & \frac{X_6}{X_2} (R_s + X_{12}) & -\frac{X_6}{X_2} X_{10} + \omega_s \\ 0 & \frac{X_9}{X_3} R_p & 0 & \frac{X_8}{X_3} R_p & -\frac{X_6}{X_2} X_{10} - \omega_s & \frac{X_6}{X_2} (R_s + X_{11}) \end{bmatrix}$$

$$\mathbf{A_{v1}} = \begin{bmatrix} -\frac{1}{L_f} & 0 & 0 & 0 \\ 0 & -\frac{1}{L_f} & 0 & 0 \\ 0 & 0 & -\frac{1}{L_f} & 0 \\ 0 & 0 & 0 & -\frac{1}{L_f} \end{bmatrix} \quad \mathbf{A_{v2}} = \begin{bmatrix} -\frac{X_5}{X_1} & 0 & \frac{X_7}{X_1} & 0 & \frac{X_5}{X_1} & 0 & -\frac{X_7}{X_1} & 0 & \frac{X_9}{X_3} & 0 & \frac{X_9}{X_3} X_{13} \\ 0 & -\frac{X_5}{X_1} & 0 & \frac{X_7}{X_1} & 0 & \frac{X_5}{X_1} & 0 & -\frac{X_7}{X_1} & 0 & \frac{X_9}{X_3} & \frac{X_9}{X_3} X_{14} \\ \frac{X_7}{X_1} & 0 & -\frac{X_4}{X_1} & 0 & -\frac{X_7}{X_1} & 0 & \frac{X_4}{X_1} & 0 & \frac{X_8}{X_3} & 0 & \frac{X_8}{X_3} X_{13} \\ 0 & \frac{X_7}{X_1} & 0 & -\frac{X_4}{X_1} & 0 & -\frac{X_7}{X_1} & 0 & \frac{X_4}{X_1} & 0 & \frac{X_8}{X_3} & \frac{X_8}{X_3} X_{14} \\ -\frac{X_9}{X_3} & 0 & -\frac{X_8}{X_3} & 0 & \frac{X_9}{X_3} & 0 & \frac{X_8}{X_3} & 0 & \frac{X_6}{X_2} & 0 & \frac{X_6}{X_2} X_{13} \\ 0 & -\frac{X_9}{X_3} & 0 & -\frac{X_8}{X_3} & 0 & \frac{X_9}{X_3} & 0 & \frac{X_8}{X_3} & 0 & \frac{X_6}{X_2} & \frac{X_6}{X_2} X_{14} \end{bmatrix}$$

$$\mathbf{A_{i3}} = \begin{bmatrix} \frac{1}{C_f} \mathbf{I_{4\times4}} & -\frac{1}{C_f} \mathbf{I_{4\times4}} & \mathbf{0_{8\times2}} \\ \mathbf{0_{4\times4}} & \frac{1}{C_p} \mathbf{I_{4\times4}} & \\ & & \frac{1}{C_s} \mathbf{I_{2\times2}} \\ \mathbf{0_{3\times8}} & & \frac{2}{\pi} \frac{1}{C_r} \frac{I_{ss}}{I_{\text{speak}}} \quad \frac{2}{\pi} \frac{1}{C_r} \frac{I_{sc}}{I_{\text{speak}}} \end{bmatrix} \quad \mathbf{A_{v3}} = \begin{bmatrix} 0 & \omega_s & 0 & 0 & 0 & 0 & 0 & 0 & 0 & 0 & 0 \\ -\omega_s & 0 & 0 & 0 & 0 & 0 & 0 & 0 & 0 & 0 & 0 \\ 0 & 0 & 0 & \omega_s & 0 & 0 & 0 & 0 & 0 & 0 & 0 \\ 0 & 0 & -\omega_s & 0 & 0 & 0 & 0 & 0 & 0 & 0 & 0 \\ 0 & 0 & 0 & 0 & 0 & \omega_s & 0 & 0 & 0 & 0 & 0 \\ 0 & 0 & 0 & 0 & -\omega_s & 0 & 0 & 0 & 0 & 0 & 0 \\ 0 & 0 & 0 & 0 & 0 & 0 & 0 & \omega_s & 0 & 0 & 0 \\ 0 & 0 & 0 & 0 & 0 & 0 & -\omega_s & 0 & 0 & 0 & 0 \\ 0 & 0 & 0 & 0 & 0 & 0 & 0 & 0 & 0 & \omega_s & 0 \\ 0 & 0 & 0 & 0 & 0 & 0 & 0 & 0 & -\omega_s & 0 & 0 \\ 0 & 0 & 0 & 0 & 0 & 0 & 0 & 0 & 0 & 0 & -\frac{1}{C_r R_L} \end{bmatrix}$$

$$\mathbf{C} = \begin{bmatrix} \frac{I_{f1s}}{I_{f\text{peak}}} & \frac{I_{f1c}}{I_{f\text{peak}}} & \frac{I_{f2s}}{I_{f\text{peak}}} & \frac{I_{f2c}}{I_{f\text{peak}}} & 0 & 0 & 0 & 0 & 0 & 0 & 0 & 0 & 0 & 0 & 0 & 0 & 0 & 0 & 0 & 0 \\ 0 & 0 & 0 & 0 & 0 & 0 & 0 & 0 & 0 & 0 & 0 & 0 & 0 & 0 & 0 & 0 & 0 & 0 & 0 & 1 \end{bmatrix}$$

$$\mathbf{B_1}=\begin{bmatrix}
-X_{15}\left(L_sV_{\mathrm{eq2}s}K_2+\sqrt{L_pL_s}V_{\mathrm{eq0}s}\right)+\frac{2X_9}{X_3^2}\left(-X_5V_{\mathrm{eq1}s}L_s+X_7L_sV_{\mathrm{eq2}s}-X_9\sqrt{L_pL_s}V_{\mathrm{eq0}s}\right)\\
-X_{15}\left(L_sV_{\mathrm{eq2}c}K_2+\sqrt{L_pL_s}V_{\mathrm{eq0}c}\right)+\frac{2X_9}{X_3^2}\left(-X_5V_{\mathrm{eq1}c}L_s+X_7V_{\mathrm{eq2}c}L_s-X_9\sqrt{L_pL_s}V_{\mathrm{eq0}c}\right)\\
-X_{15}\left(-2L_sK_1V_{\mathrm{eq2}s}+L_sV_{\mathrm{eq1}s}K_2-\sqrt{L_pL_s}V_{\mathrm{eq0}s}K_p\right)+\frac{2X_9}{X_3^2}\left(-X_4L_sV_{\mathrm{eq2}s}+X_7L_sV_{\mathrm{eq1}s}-X_8\sqrt{L_pL_s}V_{\mathrm{eq0}s}\right)\\
-X_{15}\left(-2L_sK_1V_{\mathrm{eq2}c}+L_sV_{\mathrm{eq1}c}K_2-\sqrt{L_pL_s}V_{\mathrm{eq0}c}K_p\right)+\frac{2X_9}{X_3^2}\left(-X_4L_sV_{\mathrm{eq2}c}+X_7L_sV_{\mathrm{eq1}c}-X_8\sqrt{L_pL_s}V_{\mathrm{eq0}c}\right)\\
-X_{15}\left(\sqrt{L_pL_s}V_{\mathrm{eq1}s}-K_p\sqrt{L_pL_s}V_{\mathrm{eq2}s}\right)+\frac{2X_9}{X_3^2}\left(-\sqrt{L_pL_s}X_9V_{\mathrm{eq1}s}-X_8\sqrt{L_pL_s}V_{\mathrm{eq2}s}-X_6L_pV_{\mathrm{eq0}s}\right)\\
-X_{15}\left(\sqrt{L_pL_s}V_{\mathrm{eq1}c}-K_p\sqrt{L_pL_s}V_{\mathrm{eq2}c}\right)+\frac{2X_9}{X_3^2}\left(-\sqrt{L_pL_s}X_9V_{\mathrm{eq1}c}-X_8\sqrt{L_pL_s}V_{\mathrm{eq2}c}-X_6L_pV_{\mathrm{eq0}c}\right)
\end{bmatrix}$$

$$\mathbf{B_2}=\begin{bmatrix}
-X_{15}\left(-2K_2L_sV_{\mathrm{eq1}s}+K_1L_sV_{\mathrm{eq2}s}-K_p\sqrt{L_pL_s}V_{\mathrm{eq0}s}\right)+\frac{2X_8}{X_3^2}\left(-X_5L_sV_{\mathrm{eq1}s}+X_7L_sV_{\mathrm{eq2}s}-X_9\sqrt{L_pL_s}V_{\mathrm{eq0}s}\right)\\
-X_{15}\left(-2K_2L_sV_{\mathrm{eq1}c}+K_1L_sV_{\mathrm{eq2}c}-K_p\sqrt{L_pL_s}V_{\mathrm{eq0}c}\right)+\frac{2X_8}{X_3^2}\left(-X_5L_sV_{\mathrm{eq1}c}+X_7L_sV_{\mathrm{eq2}c}-X_9\sqrt{L_pL_s}V_{\mathrm{eq0}c}\right)\\
-X_{15}\left(K_1L_sV_{\mathrm{eq1}s}+\sqrt{L_pL_s}V_{\mathrm{eq0}s}\right)+\frac{2X_8}{X_3^2}\left(-X_4L_sV_{\mathrm{eq2}s}+X_7L_sV_{\mathrm{eq1}s}-X_8\sqrt{L_pL_s}V_{\mathrm{eq0}s}\right)\\
-X_{15}\left(K_1L_sV_{\mathrm{eq1}c}+\sqrt{L_pL_s}V_{\mathrm{eq0}c}\right)+\frac{2X_8}{X_3^2}\left(-X_4L_sV_{\mathrm{eq2}c}+X_7L_sV_{\mathrm{eq1}c}-X_8\sqrt{L_pL_s}V_{\mathrm{eq0}c}\right)\\
-X_{15}\left(-K_p\sqrt{L_pL_s}V_{\mathrm{eq1}s}+\sqrt{L_pL_s}V_{\mathrm{eq2}s}\right)+\frac{2X_8}{X_3^2}\left(-X_9\sqrt{L_pL_s}V_{\mathrm{eq1}s}-X_8\sqrt{L_pL_s}V_{\mathrm{eq2}s}-X_6L_pV_{\mathrm{eq0}s}\right)\\
-X_{15}\left(-K_p\sqrt{L_pL_s}V_{\mathrm{eq1}c}+\sqrt{L_pL_s}V_{\mathrm{eq2}c}\right)+\frac{2X_8}{X_3^2}\left(-X_9\sqrt{L_pL_s}V_{\mathrm{eq1}c}-X_8\sqrt{L_pL_s}V_{\mathrm{eq2}c}-X_6L_pV_{\mathrm{eq0}c}\right)
\end{bmatrix}$$

$$\mathbf{B_3}=\begin{bmatrix}
-X_{15}\left(-L_sV_{\mathrm{eq2}s}-\sqrt{L_pL_s}V_{\mathrm{eq0}s}K_2\right)+\frac{2X_7}{X_3^2}\left(-X_5L_sV_{\mathrm{eq1}s}+X_7L_sV_{\mathrm{eq2}s}-X_9\sqrt{L_pL_s}V_{\mathrm{eq0}s}\right)\\
-X_{15}\left(-L_sV_{\mathrm{eq2}c}-\sqrt{L_pL_s}V_{\mathrm{eq0}c}K_2\right)+\frac{2X_7}{X_3^2}\left(-X_5L_sV_{\mathrm{eq1}c}+X_7L_sV_{\mathrm{eq2}c}-X_9\sqrt{L_pL_s}V_{\mathrm{eq0}c}\right)\\
-X_{15}\left(-L_sV_{\mathrm{eq1}s}-\sqrt{L_pL_s}V_{\mathrm{eq0}s}K_1\right)+\frac{2X_7}{X_3^2}\left(-X_4L_sV_{\mathrm{eq2}s}+X_7L_sV_{\mathrm{eq1}s}-X_8\sqrt{L_pL_s}V_{\mathrm{eq0}s}\right)\\
-X_{15}\left(-L_sV_{\mathrm{eq1}c}-\sqrt{L_pL_s}V_{\mathrm{eq0}c}K_1\right)+\frac{2X_7}{X_3^2}\left(-X_4L_sV_{\mathrm{eq2}c}+X_7L_sV_{\mathrm{eq1}c}-X_8\sqrt{L_pL_s}V_{\mathrm{eq0}c}\right)\\
-X_{15}\left(-K_2\sqrt{L_pL_s}V_{\mathrm{eq1}s}-K_1\sqrt{L_pL_s}V_{\mathrm{eq2}s}-2L_pK_pV_{\mathrm{eq0}s}\right)\\
+\frac{2X_7}{X_3^2}\left(-X_9\sqrt{L_pL_s}V_{\mathrm{eq1}s}-X_8\sqrt{L_pL_s}V_{\mathrm{eq2}s}-X_6L_pV_{\mathrm{eq0}s}\right)\\
-X_{15}\left(-K_2\sqrt{L_pL_s}V_{\mathrm{eq1}c}-K_1\sqrt{L_pL_s}V_{\mathrm{eq2}c}-2K_pL_pV_{\mathrm{eq0}c}\right)\\
+\frac{2X_7}{X_3^2}\left(-X_9\sqrt{L_pL_s}V_{\mathrm{eq1}c}-X_8\sqrt{L_pL_s}V_{\mathrm{eq2}c}-X_6L_pV_{\mathrm{eq0}c}\right)
\end{bmatrix}.$$

REFERENCES

[1] W. Ji, G. Jeong, J. Kim, J. Lee, and H. Lee, "Design parameter analysis of the linear induction motor for Maglev conveying system," in *Proc. 11th Int. Symp. Linear Drives Ind. Appl.*, 2017, pp. 1–3.

[2] M. Fabbri, P. L. Ribani, and D. Zuffa, "Design and testing of a magnetically levitated conveyor," *IEEE Trans. Magn.*, vol. 49, no. 1, pp. 577–585, Jan. 2013.

[3] Beckhoff Automation, "XTS with NCT," Beckhoff, 2022. [Online]. Available: https://www.beckhoff.com/en-en/products/motion/xts-with-nct

[4] B. J. Limb et al., "Economic viability and environmental impact of in-motion wireless power transfer," *IEEE Trans. Transp. Electrific.*, vol. 5, no. 1, pp. 135–146, Mar. 2019.

[5] A. Zaheer, M. Neath, H. Z. Z. Beh, and G. A. Covic, "A dynamic EV charging system for slow moving traffic applications," *IEEE Trans. Transp. Electrific.*, vol. 3, no. 2, pp. 354–369, Jun. 2017.

[6] G. Song, H. Wang, J. Zhang, and T. Meng, "Automatic docking system for recharging home surveillance robots," *IEEE Trans. Consum. Electron.*, vol. 57, no. 2, pp. 428–435, May 2011.

[7] S. Y. Choi, B. W. Gu, S. Y. Jeong, and C. T. Rim, "Advances in wireless power transfer systems for roadway-powered electric vehicles," *IEEE J. Emerg. Sel. Topics Power Electron.*, vol. 3, no. 1, pp. 18–36, Mar. 2015.

[8] C. C. Mi, G. Buja, S. Y. Choi, and C. T. Rim, "Modern advances in wireless power transfer systems for roadway powered electric vehicles," *IEEE Trans. Ind. Electron.*, vol. 63, no. 10, pp. 6533–6545, Oct. 2016.

[9] S. Y. Choi, J. Huh, W. Y. Lee, S. W. Lee, and C. T. Rim, "New cross-segmented power supply rails for roadway powered electric vehicles," *IEEE Trans. Power Electron.*, vol. 28, no. 12, pp. 5832–5841, Dec. 2013.

[10] S. Zhou and C. Mi, "Multi-paralleled LCC reactive power compensation networks and their tuning method for electric vehicle dynamic wireless charging," *IEEE Trans. Ind. Electron.*, vol. 63, no. 10, pp. 6546–6556, Oct. 2016.

[11] S. Huang, T. Lee, W. Li, and R. Chen, "Modular on-road AGV wireless charging systems via interoperable power adjustment," *IEEE Trans. Ind. Electron.*, vol. 66, no. 8, pp. 5918–5928, Aug. 2019.

[12] Y. Li et al., "A new coil structure and its optimization design with constant output voltage and constant output current for electric vehicle dynamic wireless charging," *IEEE Trans. Ind. Inform.*, vol. 15, no. 9, pp. 5244–5256, Sep. 2019.

[13] B. Song, B. Du, S. Cui, Y. Li, and C. Zhu, "Mechanism analysis of output fluctuation in a three-phase dynamic wireless charging system," *IEEE Trans. Ind. Electron.*, vol. 69, no. 3, pp. 2252–2264, Mar. 2022.

[14] V. Z. Barsari, D. J. Thrimawithana, S. Kim, and G. A. Covic, "Modular coupler with integrated planar transformer for wireless EV charging," *IEEE Trans. Power Electron.*, vol. 38, no. 7, pp. 9206–9217, Jul. 2023.

[15] J. Liu, Z. Liu, and H. Su, "Passivity-based PI control for receiver side of dynamic wireless charging system in electric vehicles," *IEEE Trans. Ind. Electron.*, vol. 69, no. 1, pp. 783–794, Jan. 2022.

[16] S. D. Zhang, C. Zhu, Y. Yin, and M. Zhang, "Composite control to suppress output fluctuation for receiver side of dynamic wireless power transfer system," *IEEE Trans. Power Electron.*, vol. 38, no. 5, pp. 6720–6733, May 2023.

[17] C. Z. Wang, K. Song, G. Wei, S. Dong, and R. G. Lu, "Primary-side control method in two-transmitter inductive wireless power transfer systems for dynamic wireless charging applications," in *Proc. IEEE PELS Workshop Emerg. Technol. Wireless Power Transfer*, 2017, pp. 1–6.

[18] Q. Zhang, X. Zhang, W. Li, T. Hu, Y. Wang, and S. Shen, "New control method for receiver-side DC-DC converter with large stability margin and fluctuation suppression toward DWPT system," *IEEE Trans. Ind. Electron.*, vol. 70, no. 8, pp. 7944–7954, Aug. 2023.

[19] Z. Zhou, L. Zhang, Z. Liu, Q. Chen, R. Long, and H. Su, "Model predictive control for the receiving-side DC–DC converter of dynamic wireless power transfer," *IEEE Trans. Power Electron.*, vol. 35, no. 9, pp. 8985–8997, Sep. 2020.

[20] H. Li, K. Wang, L. Huang, W. Chen, and X. Yang, "Dynamic modeling based on coupled modes for wireless power transfer systems," *IEEE Trans. Power Electron.*, vol. 30, no. 11, pp. 6245–6253, Nov. 2015.

[21] H. Li, J. Fang, and Y. Tang, "Dynamic phasor-based reduced-order models of wireless power transfer systems," *IEEE Trans. Power Electron.*, vol. 34, no. 11, pp. 11361–11370, Nov. 2019.

[22] S. Lee, B. Chao, and C. T. Rim, "Dynamics characterization of the inductive power transfer system for online electric vehicles by Laplace phasor transform," *IEEE Trans. Power Electron.*, vol. 28, no. 12, pp. 5902–5909, Dec. 2013.
[23] Z. U. Zahid et al., "Modeling and control of series-series compensated inductive power transfer system," *IEEE J. Emerg. Sel. Topics Power Electron.*, vol. 3, no. 1, pp. 111–123, Mar. 2015.
[24] I. Aizpuru, E. Agirrezabala, M. Mazuela, U. Iraola, E. Oyarbide, and C. Bernal, "Dynamic wireless power transfer DWPT time domain model: Xyz position and speed coupling effect," in *Proc. 24th Eur. Conf. Power Electron. Appl.*, 2022, pp. 1–9.
[25] T. Hamada, T. Fujita, and H. Fujimoto, "Fast start-up control of both-side current without overshoot focusing on rectification timing for dynamic wireless power transfer systems," *IEEE J. Emerg. Sel. Topics Ind. Electron.*, vol. 5, no. 3, pp. 1039–1047, Jul. 2024.
[26] X. Li, Y. Zhang, S. Chen, X. Zhang, and Y. Tang, "Coil relative position transient issue in wireless power transfer systems," *IEEE Trans. Ind. Electron.*, vol. 69, no. 3, pp. 2621–2630, Mar. 2022.
[27] S. Liu, J. Xu, Y. Liu, Y. Li, Y. Liu, and Z. He, "Phenomenon, modeling, and analysis of transient power impacts and oscillations in fast-moving dynamic wireless power transfer system," *IEEE Trans. Ind. Electron.*, vol. 72, no. 8, pp. 8094–8106, Aug. 2025, doi: 10.1109/TIE.2025.
[28] C. Cai, M. Saeedifard, J. Wang, P. Zhang, J. Zhao, and Y. Hong, "A cost-effective segmented dynamic wireless charging system with stable efficiency and output power," *IEEE Trans. Power Electron.*, vol. 37, no. 7, pp. 8682–8700, Jul. 2022.
[29] Y. Geng, Q. Guo, Z. Yang, F. Lin, and Y. Wang, "Design and optimization of real-time strong coupling coil of dynamic wireless power transfer for electrical vehicle," *IEEE Trans. Veh. Technol.*, vol. 72, no. 9, pp. 11495–11504, Sep. 2023.
[30] W. Zhang and C. C. Mi, "Compensation topologies of high-power wireless power transfer systems," *IEEE Trans. Veh. Technol.*, vol. 65, no. 6, pp. 4768–4778, Jun. 2016.
[31] Z. Huang, S. C. Wong, and C. K. Tse, "Design of a single-stage inductive-power-transfer converter for efficient EV battery charging," *IEEE Trans. Veh. Technol.*, vol. 66, no. 7, pp. 5808–5821, Jul. 2017.
[32] L. Yang, X. Li, S. Liu, Z. Xu, and C. Cai, "Analysis and design of an LCCC/S-compensated WPT system with constant output characteristics for battery charging applications," *IEEE J. Emerg. Sel. Topics Power Electron.*, vol. 9, no. 1, pp. 1169–1180, Feb. 2021.
[33] X. Dai, J.-C. Jiang, and J.-Q. Wu, "Charging area determining and power enhancement method for multiexcitation unit configuration of wirelessly dynamic charging EV system," *IEEE Trans. Ind. Electron.*, vol. 66, no. 5, pp. 4086–4096, May 2019.
[34] E. X. Yang, F. C. Lee, and M. M. Jovanovic, "Small-signal modeling of series and parallel resonant converters," in *Proc. 7th Annu. Appl. Power Electron. Conf. Expo.*, 1992, pp. 785–792.
[35] S. Tian, F. C. Lee, and Q. Li, "A simplified equivalent circuit model of series resonant converter," *IEEE Trans. Power Electron.*, vol. 31, no. 5, pp. 3922–3931, May 2016.
[36] C. Buccella, C. Cecati, H. Latafat, P. Pepe, and K. Razi, "Observer-based control of LLC DC/DC resonant converter using extended describing functions," *IEEE Trans. Power Electron.*, vol. 30, no. 10, pp. 5881–5891, Oct. 2015.
[37] C. Zhu et al., "A magnetic field concentration enhanced I-shaped transmitter for DWPT system to achieve low power fluctuation," *IEEE Trans. Power Electron.*, vol. 39, no. 1, pp. 1690–1700, Jan. 2024.

Junyi Ji received the B.S. degree in mechanical engineering from Shanghai Jiao Tong University, Shanghai, China, in 2023. He is currently working toward the master's degree in mechanical engineering from Shanghai Jiao Tong University, Shanghai, China.

His research interests include dynamic wireless power transfer and its application in linear transport systems, and high-power wireless power transfer system.

Chong Zhu (Member, IEEE) received the B.S. degree from the China University of Mining and Technology, Xuzhou, China, in 2010, and the Ph.D. degree from Zhejiang University, Hangzhou, China, in 2016, both in electrical engineering.

He was a Postdoctoral Researcher with San Diego State University, San Diego, CA, USA, from 2017 to 2019. He is currently an Associate Professor with the School of Mechanical Engineering, Shanghai Jiao Tong University, Shanghai, China. His research interests include inductive power transfer, wide bandgap devices, and thermal management in electric vehicles.

Jia Li (Graduate Student Member, IEEE) received the B.S. degree in mechanical engineering in 2020 from the Shanghai Jiao Tong University, Shanghai, China, where he is currently working toward the Ph.D. degree in mechanical engineering.

His research interests include wireless power transfer and its application in autonomous underwater vehicles, and power system stability and control.

Jixie Xie received the B.S. degree in energy and power engineering from Southeast University, Nanjing, China, in 2017, and the M.Sc. degree in materials for energy and environment from University College London, London, U.K., in 2018. He is currently working toward the Ph.D. degree in mechanical engineering with the Shanghai Jiao Tong University, Shanghai, China.

His current research interests include wireless power transfer, magnetic shielding design, and resonant couplers optimization in autonomous underwater vehicles.

Xi Zhang (Senior Member, IEEE) received the bachelor's, master's, and Ph.D. degrees in electrical engineering from Shanghai Jiao Tong University, Shanghai, China, in 2002, 2004, and 2007, respectively.

He joined the University of Michigan-Dearborn, USA, as a Post doctor in 2007 and a Research Scientist in 2009. He is currently a Full Professor and a Doctoral Supervisor with the Institute of Intelligent Vehicles, Shanghai Jiao Tong University. His research interests include EV electric drive systems, battery management systems, wireless power transfer technologies, etc. He has published three books and around 130 research papers. He was granted over 50 patents of invention.

Dr. Zhang was sponsored by Shanghai Pujiang Talent Program and won Chinese Industry-University-Institute Cooperation Promotion Award (Individual) in 2016. He was the recipient of the Second Prize of Science and Technology Progress Award of China Society of Automotive Engineering in 2022. He is currently a New Energy Power Conversion Technology Committee Member of China Power Supply Society. He was the Chair, Program Committee Chair, or Section Chair for several international academic conferences.